

UTOPYA: A Multimodal Deep Learning Framework for Physics-Informed Anomaly Detection and Time-Series Prediction

Robson W. S. Pessoa^{a,*}, Julien Amblard^b, Alessandra Russo^b, Idelfonso
B.R. Nogueira^{a,*}

^a*Department of Chemical Engineering, Norwegian University of Science and Technology
(NTNU), Trondheim, Norway*

^b*Department of Computing, Imperial College London, London, United Kingdom*

Abstract

Anomaly detection in batch processes is hindered by transient dynamics, scarce fault labels, and reliance on single-modality sensor data. This work introduces UTOPYA (Unified Temporal Observation for Physics-Informed Anomaly Detection and Time-Series Prediction), a 15.2M-parameter multimodal framework that jointly addresses anomaly detection, time-series prediction, and phase classification in batch distillation by fusing eight data modalities through Feature-wise Linear Modulation (FiLM) conditioned cross-modal attention and gated fusion. A physics-informed regularisation scheme introduced in this work enforces temporal smoothness and thermodynamic monotonicity, while curriculum learning introduces training samples in order of physical difficulty. On the 119-experiment multimodal batch distillation dataset of [Arweiler et al. \(2026\)](#), UTOPYA achieves a window-level test AUROC of 0.832 and 0.874 under multi-signal experiment-level scoring, substantially outperforming four external baselines (PCA, autoencoder, Isolation Forest, and LSTM autoencoder) evaluated under identical conditions (+0.147 window-level AUROC over the best baseline). A multimodal ablation over 15 architectural configurations shows that static context via FiLM conditioning is the key enabler, lifting experiment-level multi-signal AUROC by +0.145 over the unimodal baseline (0.729 to 0.874). Separately, a

*Corresponding author

Email address: `idelfonso.nogueira@ntnu.no` (Idelfonso B.R. Nogueira)

training ablation across 14 design choices reveals that several widely-adopted techniques, including instance normalisation, Mixup, ensembling, test-time augmentation, and stochastic weight averaging, fail to improve or actively degrade generalisation in this data-scarce setting. These negative results expose a fundamental tension between smoothing-based regularisation and anomaly detection, providing practical guidance for multimodal process monitoring deployment.

Keywords: anomaly detection, batch distillation, multimodal deep learning, physics-informed neural networks, temporal convolutional networks, curriculum learning, process monitoring

1. Introduction

Detecting anomalous operation in industrial processes is a long-standing challenge for the process engineering community. Classical statistical process monitoring relies on multivariate methods such as Principal Component Analysis and Partial Least Squares (Ge et al., 2013; Venkatasubramanian et al., 2003a), which establish a model of normal operating conditions and flag deviations through monitoring statistics. While effective for steady-state continuous processes, these methods struggle when the process is inherently transient, because the normal operating envelope itself changes with time.

The challenge becomes even more acute when anomaly detection is coupled with simultaneous time-series prediction. One approach to detect faults is to predict future sensor trajectories and compare them against observed values; a well-calibrated predictive model will produce large residuals precisely when the process deviates from expected behaviour. However, this is particularly challenging in transient systems. Temperatures, pressures, and compositions evolve non-stationarily through distinct phases, so the model must learn phase-dependent dynamics rather than a single stationary pattern (Venkatasubramanian et al., 2003b).

Several studies have applied data-driven deep learning methods to process fault detection (Wang et al., 2018; Choi et al., 2021; Pang et al., 2021; Aldrich and Auret, 2020). Among those methods, autoencoders, variational autoencoders, and recurrent neural networks have been applied to learn representations of normal behaviour and flag deviations. These methods are almost exclusively benchmarked on continuous processes using a single data modality, most commonly time-series sensor readings on standard problems

such as the Tennessee Eastman Process (Downs and Vogel, 1993). Two limitations persist. Purely data-driven models tend to overfit when labelled fault data is scarce, and single-modality approaches discard information from other sensing channels.

Two sources of complementary knowledge can help overcome these limitations. First, *multimodal fusion* enables the model to exploit heterogeneous data streams—process sensors, visual inspection, acoustic signatures, spectroscopic analysis—that are individually informative but collectively richer (Baltrušaitis et al., 2019; Gao et al., 2020). This is what human operators routinely do when diagnosing faults. In the chemical process industry, Process Analytical Technology has driven the adoption of diverse sensing modalities (Simon et al., 2015). However, data from different instruments are still typically analysed by separate domain-specific models (Ge et al., 2013; Jiang et al., 2023). Fusion strategies can overcome this separation, ranging from early concatenation of raw features to intermediate-level interaction of learned representations (Baltrušaitis et al., 2019). Recent conditioning mechanisms such as Feature-wise Linear Modulation (FiLM; Perez et al., 2018) offer a way to modulate dynamic features with static contextual information.

Second, *physics-informed regularization* encodes domain knowledge as soft constraints in the loss function (Raissi et al., 2019). Physics-informed neural networks (PINNs) have been applied in chemical engineering to reaction kinetics, transport phenomena, and process optimisation. The underlying principle — that physical processes are governed by conservation equations that impose continuity on state variables — translates naturally to batch distillation, where thermal and hydraulic inertia ensure that temperatures, pressures, and flow rates evolve smoothly over time. The specific physics-informed formulation introduced in this work, which combines temporal smoothness and thermodynamic monotonicity as soft constraints on predicted trajectories, is described in Section 3.6.

Despite substantial work in both areas, no prior study jointly exploits multimodal fusion and physics-informed regularization for anomaly detection in batch processes. Batch distillation is a workhorse unit operation in the chemical and pharmaceutical industries (Diwekar, 1995; Stichlmair and Fair, 2010). It is valued for its flexibility in separating multicomponent mixtures without a continuous feed, but its transient dynamics across startup, operation, and shutdown phases make steady-state monitoring tools inadequate. Labelled fault data is difficult to obtain. Deliberately inducing anomalies on production equipment is costly and real faults are rare events (Crowl and

Louvar, 2019).

The recently published dataset of [Arweiler et al. \(2026\)](#) opens precisely this opportunity. It comprises 119 experiments on a laboratory-scale distillation plant, covering eight data modalities (time-series, images, audio, video, NMR spectra, GC analysis, tabular metadata, and text logs) and including in total around 86.3 GB of raw data across three chemical systems. Each anomalous experiment is paired with a fault-free reference conducted under identical nominal conditions, providing a rigorous evaluation framework. To the best of our knowledge, this is the first dataset to offer paired normal and anomalous batch distillation experiments with multimodal coverage.

In this work, we present **UTOPYA** (**U**nified **T**emporal **O**bservation for **P**hysics-informed **A**nomaly detection and time-series prediction), a multimodal framework that jointly addresses anomaly detection, time-series prediction, and phase classification in industrial batch processes. UTOPYA integrates two complementary forms of domain knowledge: a physics-informed regularisation scheme that enforces temporal smoothness and thermodynamic monotonicity in predicted time series; and curriculum learning, which introduces training samples in order of physical difficulty to improve generalisation in data-scarce settings. Our contributions are:

1. UTOPYA, a multimodal deep learning architecture that fuses eight data modalities via FiLM conditioning, bidirectional cross-modal attention, and gated fusion with graceful degradation for absent modalities, under a multi-task objective spanning anomaly detection, time-series prediction, and phase classification.
2. A physics-informed regularisation scheme for batch distillation that encodes temporal smoothness and distillation column temperature profile monotonicity constraints as soft penalties on predicted trajectories.
3. A curriculum learning strategy that exploits the natural difficulty hierarchy of anomaly detection in batch processes, combined with self-supervised pretraining using block masking and contrastive learning, and per-experiment normalisation that removes operating-point-specific baselines to improve cross-experiment generalisation.
4. A systematic ablation study comprising both a multimodal ablation that isolates the contribution of each data modality (time-series, GC, audio, static context) and a training ablation spanning 14 design decisions, providing quantitative evidence on which techniques improve generalization and which do not, including important negative results

(RevIN, Mixup, ensembling, test-time augmentation, stochastic weight averaging) and the discovery of an inverse val–test correlation that curriculum learning partially resolves.

5. A comparison with four external baselines (PCA, feedforward autoencoder, Isolation Forest, and LSTM autoencoder) evaluated under identical conditions, demonstrating that UTOPIA substantially outperforms standard methods on this challenging dataset.

The remainder of this paper is organised as follows. Section 2 describes the Arweiler et al. dataset. Section 3 details the UTOPIA architecture and training methodology. Section 4 presents the experimental setup. Section 5 reports results, ablation findings, and negative results. Section 6 concludes with lessons learned and directions for future work.

2. Dataset

We employ the multimodal batch distillation dataset published by [Arweiler et al. \(2026\)](#), available on Zenodo (record 18771181). This dataset was collected on a laboratory-scale batch distillation plant and comprises 119 experiments across three chemical systems, summarised in Table 1.

Table 1: Chemical systems in the Arweiler et al. (2025) dataset.

System	Components	Experiments
Ternary I	butan-1-ol + propan-2-ol + water	~91
Ternary II	acetone + butan-1-ol + methanol	~14
Binary	ethanol + propan-2-ol	~14

The total dataset size is approximately 86.3 GB, distributed across eight modalities:

1. **Time-series process variables:** 19 sensors and 13 actuators sampled at 1 Hz, including temperatures at multiple column positions, pressures, flow rates, liquid levels, and control valve states.
2. **Images:** Three camera streams capturing the column, reboiler, and condenser regions.
3. **Audio:** Acoustic recordings from the plant environment.
4. **Video:** Continuous video recordings of column operation.

5. **NMR spectra:** Nuclear magnetic resonance spectra of product samples collected at discrete intervals.
6. **GC analysis:** Gas chromatography composition measurements.
7. **Static tabular features:** Experiment-level metadata including operating conditions, equipment configuration, and chemical system properties.
8. **Text metadata:** Textual descriptions of experimental conditions, observations, and operator notes.

Three phases define each experiment. The *Startup* phase covers equipment heat-up and stabilization, while *Operation* corresponds to active distillation with product collection; finally, *Shutdown* involves controlled cooling and depressurization. To study anomaly detection, some experiments feature intentionally induced faults—reflux interruptions, heating power reductions, or feed composition perturbations, among others. Each anomalous experiment is paired with a fault-free reference run conducted under identical nominal conditions, enabling direct comparison.

3. Methodology

The UTOPYA architecture consists of five stages: (1) modality-specific encoding, (2) static context aggregation with FiLM conditioning, (3) bidirectional cross-modal attention, (4) gated fusion with graceful degradation, and (5) multi-task output heads with physics-informed regularization. The complete architecture is illustrated in Figure 1. UTOPYA has 15.2M trainable parameters with a shared embedding dimension of $d_{\text{model}} = 128$.

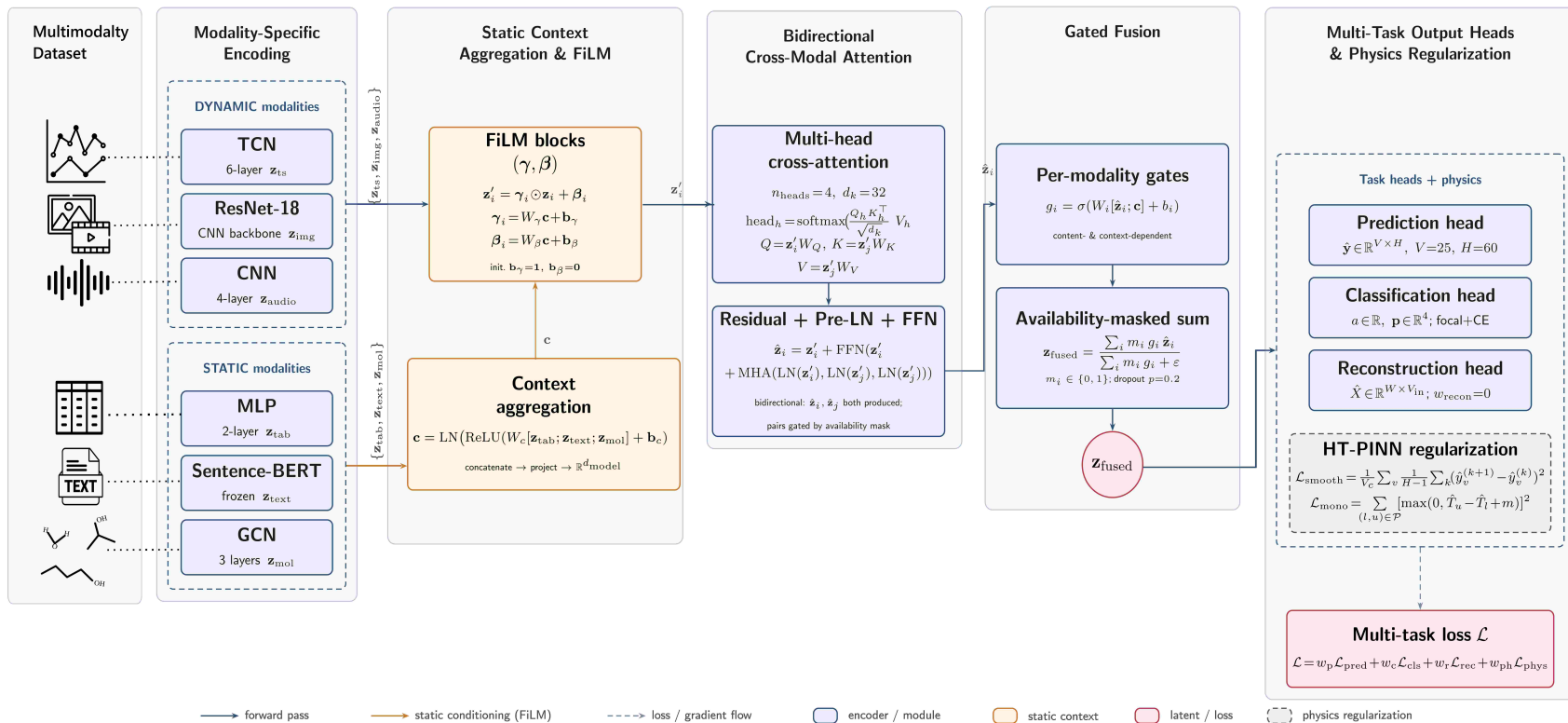


Figure 1: The UTOPIYA architecture. Dynamic modalities are encoded by dedicated networks and conditioned via FiLM using a static context vector c aggregated from tabular, text, and molecular graph encoders. Conditioned embeddings undergo bidirectional cross-modal attention and context-aware gated fusion to produce a latent vector z that feeds three task heads. The multi-task loss $\mathcal{L} = \alpha \mathcal{L}_{\text{pred}} + \beta \mathcal{L}_{\text{class}} + \gamma \mathcal{L}_{\text{recon}} + \delta \mathcal{L}_{\text{physics}}$ is augmented with physics-informed regularisation (Section 3.6).

3.1. Architecture Overview

UTOPYA processes two categories of modalities: *dynamic* modalities that vary within an experiment (time-series, images, audio, video) and *static* modalities that are fixed per experiment (tabular features, text metadata, molecular graphs). Static modalities are aggregated into a context vector that conditions dynamic modality embeddings via FiLM. The conditioned dynamic embeddings undergo bidirectional cross-modal attention before being combined through gated fusion. Three output heads (prediction, classification, and reconstruction) operate on the fused representation under a multi-task loss augmented with physics-informed regularization.

3.2. Modality Encoders

Each modality demands its own encoder. Uniform encoding is challenging because each data type—time-series, images, audio, tabular records, free text, and molecular graphs—has a fundamentally different structure, and the encoder must respect the inductive biases that come with each format while still producing compatible representations for the downstream fusion stage. However, all encoders project to a shared $d_{\text{model}} = 128$. We describe each one below.

The primary modality is time-series process data. It comprises 29 variables: 5 manipulated inputs and 24 measured outputs that include temperatures, pressures, flow rates, liquid levels, and valve states, all sampled at 1 Hz over a window of $T = 120$ timesteps. We select a Temporal Convolutional Network (TCN); (Bai et al., 2018) over recurrent alternatives. The reasons are threefold: dilated causal convolutions give an exponentially growing receptive field without the vanishing-gradient issues that plague RNNs; the entire window can be processed in parallel, which improves training throughput; and the inductive bias toward local temporal patterns suits dense process data sampled at regular intervals.

The TCN consists of $L = 6$ residual blocks, each containing a causal 1-D convolution with kernel size $k = 3$ and dilation factor $d_l = 2^{l-1}$ for layer $l \in \{1, \dots, 6\}$. The receptive field is therefore $R = 1 + 2(k - 1) \sum_{l=0}^{L-1} 2^l = 127$ timesteps, closely matching the input window. Formally, the dilated convolution at layer l computes

$$\mathbf{h}_l^{(t)} = \text{ReLU} \left(\sum_{j=0}^{k-1} \mathbf{w}_l^{(j)} \mathbf{h}_{l-1}^{(t-j \cdot d_l)} + \mathbf{b}_l \right), \quad (1)$$

where $\mathbf{W}_l^{(j)} \in \mathbb{R}^{d_{\text{model}} \times d_{\text{model}}}$ are the learned filters and the input to the first layer is a linear projection of the raw 29-dimensional signal. Each block applies weight normalisation (Salimans and Kingma, 2016), ReLU activation, and dropout ($p = 0.5$), with a skip connection $\mathbf{h}_l = \mathbf{h}_l + \mathbf{h}_{l-1}$ (after dimension matching when needed).

The encoder produces both a pooled embedding $\mathbf{z}_{\text{ts}} = \frac{1}{T} \sum_{t=1}^T \mathbf{h}_L^{(t)} \in \mathbb{R}^{d_{\text{model}}}$ (via global average pooling) and a per-timestep feature map $\mathbf{Z}_{\text{ts}} \in \mathbb{R}^{T \times d_{\text{model}}}$ used by the prediction and reconstruction heads.

Three cameras capture the column, reboiler, and condenser regions, providing visual evidence of liquid levels, foaming, flooding, and colour changes that correlate with composition. We use a shared ResNet-18 backbone (He et al., 2016) pretrained on ImageNet, which provides strong low-level feature extraction without requiring the large labelled image datasets that training from scratch would demand. Each camera frame $\mathbf{I}_c \in \mathbb{R}^{224 \times 224 \times 3}$ is processed independently through the convolutional trunk to produce a 512-dimensional feature vector, which is then projected to d_{model} via a learned linear layer. The three camera embeddings are aggregated via mean pooling:

$$\mathbf{z}_{\text{img}} = \frac{1}{3} \sum_{c=1}^3 \mathbf{W}_{\text{img}} f_{\text{ResNet}}(\mathbf{I}_c) + \mathbf{b}_{\text{img}}, \quad (2)$$

where $\mathbf{W}_{\text{img}} \in \mathbb{R}^{d_{\text{model}} \times 512}$. Mean pooling was chosen over concatenation to keep the embedding dimension fixed regardless of the number of active cameras, supporting graceful degradation when a camera is unavailable.

Acoustic recordings capture boiling intensity, vapour flow turbulence, and mechanical vibrations that change during anomalous operation (e.g., column flooding produces a distinctive low-frequency rumble). The raw waveform is converted to a log-mel spectrogram ($n_{\text{mels}} = 64$, hop length 512 samples) and processed by a 4-layer convolutional neural network with batch normalisation and max-pooling, followed by global average pooling and a linear projection to produce $\mathbf{z}_{\text{audio}} \in \mathbb{R}^{d_{\text{model}}}$. This lightweight architecture is appropriate given the relatively low information density of the audio channel compared to the time-series data.

Experiment-level metadata (operating conditions, equipment configuration, chemical system identifiers) form a high-dimensional but static feature vector $\mathbf{x}_{\text{tab}} \in \mathbb{R}^{d_{\text{tab}}}$, where d_{tab} varies between 602 and 606 depending on the chemical system. A two-layer MLP with ReLU activations and dropout

processes this vector:

$$\mathbf{z}_{\text{tab}} = \mathbf{W}_2 \text{ReLU}(\mathbf{W}_1 \mathbf{x}_{\text{tab}} + \mathbf{b}_1) + \mathbf{b}_2, \quad (3)$$

with $\mathbf{W}_1 \in \mathbb{R}^{256 \times d_{\text{tab}}}$ and $\mathbf{W}_2 \in \mathbb{R}^{d_{\text{model}} \times 256}$. Dimensionality reduction is the first role of this MLP. However, it also acts as a non-linear feature extractor, and this second role is arguably more important: the non-linearity lets the network discover interactions among operating parameters—for instance, how reflux ratio and heating power jointly affect column stability—that a simple linear projection would miss entirely, which matters when the downstream task depends on precisely those coupled effects.

Numerical sensors alone miss important semantic context. Operator notes such as “reflux interrupted at minute 15” or “unusual colour observed” carry information about the experiment that is difficult to extract from raw signals, and losing this information would leave the model blind to events that operators routinely record in their logs. We therefore encode these free-text fields into 384-dimensional embeddings with a pre-trained Sentence-BERT model (Reimers and Gurevych, 2019) and project them to the shared space:

$$\mathbf{z}_{\text{text}} = \mathbf{W}_{\text{text}} \text{SBERT}(\text{text}) + \mathbf{b}_{\text{text}}, \quad (4)$$

where $\mathbf{W}_{\text{text}} \in \mathbb{R}^{d_{\text{model}} \times 384}$. Using a frozen pre-trained language model avoids fine-tuning on the very small text corpus available.

The chemical identity of the mixture components influences expected process behaviour (e.g., azeotrope formation, relative volatilities). Molecular structures are represented as SMILES¹ strings, converted to graphs where atoms are nodes and bonds are edges, and processed by a Graph Convolutional Network (GCN; Kipf and Welling, 2017) with $K = 3$ message-passing layers (Gilmer et al., 2017). At each layer k , node features are updated according to

$$\mathbf{h}_v^{(k)} = \text{ReLU} \left(\mathbf{W}^{(k)} \sum_{u \in \mathcal{N}(v) \cup \{v\}} \frac{\mathbf{h}_u^{(k-1)}}{\sqrt{|\mathcal{N}(u)| |\mathcal{N}(v)|}} \right), \quad (5)$$

¹Simplified Molecular Input Line Entry System (SMILES) is a notation that encodes molecular structures as short ASCII strings, widely adopted in cheminformatics and machine learning on molecules.

where $\mathcal{N}(v)$ denotes the neighbours of atom v . Global mean pooling over all nodes yields $\mathbf{z}_{\text{mol}} \in \mathbb{R}^{d_{\text{model}}}$, capturing a graph-level representation of the molecular identity.

3.3. FiLM Conditioning

The same sensor reading can have different implications depending on the experimental context. For instance, a column top temperature of 80°C is expected when distilling a water-rich ternary mixture but would be anomalous for an ethanol-propanol binary system. Static modalities (tabular features, text metadata, molecular graphs) encode this experiment-level context, and thus the dynamic modality representations must be adapted accordingly.

We adopt Feature-wise Linear Modulation (FiLM; Perez et al., 2018) over simpler alternatives such as concatenation or additive conditioning. FiLM applies a learned *channel-wise* affine transformation, which lets the context selectively amplify, suppress, or shift individual feature dimensions without increasing the embedding size. This is more expressive than additive conditioning while remaining computationally lightweight.

We first aggregate the three static embeddings into a single context vector via concatenation and non-linear projection:

$$\mathbf{c} = \text{LN}(\text{ReLU}(\mathbf{W}_c[\mathbf{z}_{\text{tab}}; \mathbf{z}_{\text{text}}; \mathbf{z}_{\text{mol}}] + \mathbf{b}_c)), \quad (6)$$

where $\mathbf{c} \in \mathbb{R}^{d_{\text{model}}}$, $\mathbf{W}_c \in \mathbb{R}^{d_{\text{model}} \times 3d_{\text{model}}}$, and LN denotes layer normalisation (Ba et al., 2016). Why concatenation and not mean pooling? Mean pooling would discard chemical system specific features before the projection has a chance to weight them, and in preliminary experiments this loss of information hurts performance on the smaller chemical systems. Thus, concatenation preserves the full information from all three static sources, and the non-linear projection compresses it into a single context vector while the layer normalisation stabilises its scale.

Each dynamic modality embedding \mathbf{z}_i (for $i \in \{\text{ts}, \text{img}, \text{audio}\}$) is then modulated by context-dependent scale and shift parameters:

$$\mathbf{z}'_i = \gamma_i \odot \mathbf{z}_i + \beta_i, \quad \text{where} \quad \gamma_i = \mathbf{W}_\gamma \mathbf{c} + \mathbf{b}_\gamma, \quad \beta_i = \mathbf{W}_\beta \mathbf{c} + \mathbf{b}_\beta, \quad (7)$$

with $\mathbf{W}_\gamma, \mathbf{W}_\beta \in \mathbb{R}^{d_{\text{model}} \times d_{\text{model}}}$, and \odot denoting element-wise multiplication. Feature gating is controlled by γ_i : values near zero suppress a dimension, while values greater than one amplify it. The shift β_i introduces context-dependent bias. One detail matters for training stability. We initialise $\mathbf{b}_\gamma = \mathbf{1}$

and $\mathbf{b}_\beta = \mathbf{0}$ so that at the start FiLM performs an identity transform—this preserves the pretrained encoder representations until the conditioning parameters have had enough gradient updates to produce meaningful modulations, and without this initialisation the pretrained features degrade rapidly during the first few epochs of joint training.

3.4. Cross-Modal Attention and Gated Fusion

The dynamic embeddings are now contextually informed—but still isolated. A temperature spike coinciding with a visual change in the column, for instance, would remain invisible to any single encoder acting alone, because such complementary patterns span modalities that have not yet exchanged information with each other. We address this with cross-modal attention.

The cross-modal attention operates pairwise. For each ordered pair (i, j) of available modalities with $i \neq j$, modality i attends to modality j by supplying the queries while the attended modality contributes keys and values, following the standard scaled dot-product multi-head attention of Vaswani et al. (2017):

$$\mathbf{Q} = \mathbf{z}'_i \mathbf{W}^Q, \quad \mathbf{K} = \mathbf{z}'_j \mathbf{W}^K, \quad \mathbf{V} = \mathbf{z}'_j \mathbf{W}^V, \quad (8)$$

where $\mathbf{W}^Q, \mathbf{W}^K, \mathbf{W}^V \in \mathbb{R}^{d_{\text{model}} \times d_{\text{model}}}$. The attention output for head h is

$$\text{head}_h = \text{softmax}\left(\frac{\mathbf{Q}_h \mathbf{K}_h^\top}{\sqrt{d_k}}\right) \mathbf{V}_h, \quad (9)$$

with $d_k = d_{\text{model}}/n_{\text{heads}}$. Four attention heads are used, allowing the model to attend to different aspects of cross-modal interactions simultaneously; each head operates on a projected subspace of dimension $d_{\text{model}}/n_{\text{heads}} = 32$, so the full head stack preserves the 128-dimensional bottleneck width (Vaswani et al., 2017). This design enables the model to jointly capture multiple distinct cross-modal interaction patterns—such as temporal co-variation, anomaly-indicative divergence, and phase-dependent modulation—within a single attention layer. Their outputs are concatenated and projected through $\mathbf{W}^O \in \mathbb{R}^{d_{\text{model}} \times d_{\text{model}}}$ to produce $\text{MHA}(\mathbf{z}'_i, \mathbf{z}'_j)$ —a single vector that summarises what modality i learned from modality j across all four attention heads simultaneously. A residual connection with pre-layer normalisation then yields the updated embedding:

$$\hat{\mathbf{z}}_i = \mathbf{z}'_i + \text{FFN}\left(\mathbf{z}'_i + \text{MHA}(\text{LN}(\mathbf{z}'_i), \text{LN}(\mathbf{z}'_j), \text{LN}(\mathbf{z}'_j))\right), \quad (10)$$

where FFN is a two-layer feed-forward network with ReLU activation and hidden dimension $4d_{\text{model}}$, and LN denotes layer normalisation. The attention is *bidirectional*—both $\hat{\mathbf{z}}_i$ and $\hat{\mathbf{z}}_j$ are computed. Only one layer of cross-attention is applied. Furthermore, it is restricted to modality pairs whose availability mask is active, since attending to uninformative default embeddings injected noise into the fused representation and hurt downstream classification.

The per-pair attention output $\text{MHA}(\mathbf{z}'_i, \mathbf{z}'_j)$ summarises what modality i learned from modality j across all four heads. Although the present work uses these vectors only as inputs to the gated fusion layer, they carry structural information that could support symbolic-level explainability: attention magnitudes per modality pair indicate which channels were informative for a given prediction, and the per-head decomposition could be inspected to identify reusable interaction patterns (e.g. “audio attends to time-series during flooding events”). Extracting such symbolic rules from the trained attention maps—and combining them with the cluster-level diagnostics of Section 5.5—is left as future work and discussed further in Section 5.9.

The attended embeddings must now be combined into one vector. Averaging would be the simplest option, but it ignores the fact that different modalities are informative to different degrees depending on the specific input sample—for a particular experiment the audio channel may carry more diagnostic value than the images, or vice versa. Thus, we use learned sigmoid gates:

$$g_i = \sigma(\mathbf{W}_i[\hat{\mathbf{z}}_i; \mathbf{c}] + \mathbf{b}_i), \quad \mathbf{z}_{\text{fused}} = \frac{\sum_{i=1}^N m_i \cdot g_i \cdot \hat{\mathbf{z}}_i}{\sum_{i=1}^N m_i \cdot g_i + \epsilon}, \quad (11)$$

where $\mathbf{W}_i \in \mathbb{R}^{1 \times 2d_{\text{model}}}$ projects the concatenation of the attended embedding and context vector to a scalar gate, $m_i \in \{0, 1\}$ is the availability mask, σ is the sigmoid, and $\epsilon = 10^{-8}$ prevents division by zero. The gates are input-dependent. Because g_i depends on both the modality content $\hat{\mathbf{z}}_i$ and the static context \mathbf{c} , the model can learn, for instance, to up-weight audio when the operator notes mention a noisy environment—a behaviour that would not be possible with fixed fusion weights. Furthermore, the mask m_i zeros out any absent modality before the weighted sum so that the denominator renormalises automatically; this guarantees that the fused vector remains well-scaled at inference time regardless of how many modalities happen to be present for a given experiment.

In practice, not all modalities are available for every window (e.g. cam-

era frames are captured only intermittently and audio recordings are not available on every experiment). To ensure robustness, we employ three complementary mechanisms: (i) *modality dropout* during training, where each non-essential modality is independently masked with probability $p = 0.2$ (the time-series modality, being the primary information source, is never dropped); (ii) *learned default embeddings* $\mathbf{d}_i \in \mathbb{R}^{d_{\text{model}}}$ that are substituted for any absent modality, initialised to zero and trained end-to-end; and (iii) *availability-masked renormalisation* in the gated fusion denominator (Eq. 11), which ensures that the fused vector is properly scaled regardless of how many modalities are present.

3.5. Output Heads and Multi-Task Loss

The fused representation $\mathbf{z}_{\text{fused}}$ feeds three output heads:

An MLP projects the fused embedding to per-variable predictions: $\hat{\mathbf{y}} \in \mathbb{R}^{V \times H}$, where $V = 25$ target variables and $H = 60$ future timesteps (1 minute horizon at 1 Hz). The 25 target variables are the continuous process measurements (temperatures, pressures, flow rates, and liquid levels); the 4 binary valve states are excluded from the prediction targets because they change discontinuously and are better handled by the classification head. Each variable has a dedicated output projection to accommodate heterogeneous scales and dynamics.

A two-layer MLP with hidden dimension 128 and dropout produces two outputs: (i) a binary anomaly logit $a \in \mathbb{R}$, and (ii) phase classification logits $\mathbf{p} \in \mathbb{R}^4$ for four operational phases (normal, blind, anomalous, recovery).

A decoder reconstructs the input time-series window $\hat{\mathbf{X}} \in \mathbb{R}^{W \times V_{\text{in}}}$ from the fused representation, where $W = 120$ is the window size and $V_{\text{in}} = 29$ is the number of input variables.

The four output heads are supervised jointly through a weighted sum of four task-specific losses:

$$\mathcal{L} = w_{\text{pred}} \mathcal{L}_{\text{pred}} + w_{\text{class}} \mathcal{L}_{\text{class}} + w_{\text{recon}} \mathcal{L}_{\text{recon}} + w_{\text{phys}} \mathcal{L}_{\text{phys}}, \quad (12)$$

with fixed weights $w_{\text{pred}} = 0.1$, $w_{\text{class}} = 2.0$, $w_{\text{recon}} = 0.0$ (the reconstruction head is disabled in the production model; we report the ablation that motivates this choice in Section 5.6), and $w_{\text{phys}} = 0.5$. We adopt fixed weights rather than learnable uncertainty weighting (Kendall et al., 2018): the ablation study reported in Section 5.6 compares both schemes and reveals that, in our data-scarce setting, the prediction loss tends to dominate when weights

are learned, degrading anomaly detection performance. The four component losses are defined below; the physics loss is deferred to Section 3.6.

Prediction loss. The prediction head emits per-variable trajectories $\hat{y}_v^{(k)}$ over the $H = 60$ -step horizon. Continuous variables (temperatures, pressures, flow rates, liquid levels; $V_c = 21$) are supervised with mean-squared error against the ground truth $y_v^{(k)}$, and binary valve states ($V_b = 4$) are supervised with binary cross-entropy on the same horizon, so that prediction errors on valve switching contribute on the same scale as continuous residuals:

$$\mathcal{L}_{\text{pred}} = \frac{1}{V_c H} \sum_{v=1}^{V_c} \sum_{k=1}^H (\hat{y}_v^{(k)} - y_v^{(k)})^2 + \frac{1}{V_b H} \sum_{v=1}^{V_b} \sum_{k=1}^H \text{BCE}(\hat{y}_v^{(k)}, y_v^{(k)}). \quad (13)$$

The total of $V_c + V_b = 25$ target variables corresponds to the prediction-MAE column of Table 4.

Classification loss. The classification head produces (i) a binary anomaly logit a that is trained against the binary anomaly label $y \in \{0, 1\}$ and (ii) phase logits $\mathbf{p} \in \mathbb{R}^4$ trained against the phase label $c \in \{1, \dots, 4\}$. The total classification loss is the sum of an anomaly-focal term and a phase cross-entropy term:

$$\mathcal{L}_{\text{class}} = \mathcal{L}_{\text{focal}} + \mathcal{L}_{\text{phase}}, \quad (14)$$

$$\mathcal{L}_{\text{focal}} = -w_y (1 - p_t)^{\gamma_f} \log p_t, \quad p_t = \begin{cases} \sigma(a) & \text{if } y = 1, \\ 1 - \sigma(a) & \text{if } y = 0, \end{cases} \quad (15)$$

$$\mathcal{L}_{\text{phase}} = - \sum_{j=1}^4 \mathbb{1}\{c = j\} \log \frac{\exp(p_j)}{\sum_{i=1}^4 \exp(p_i)}, \quad (16)$$

where $\sigma(\cdot)$ is the sigmoid, $\gamma_f = 2.0$ is the focal focusing parameter (Lin et al., 2017), and the per-sample weight is $w_y = w_+ = 6.0$ for anomalous windows and $w_y = 1.0$ for normal windows. The value $w_+ = 6.0$ compensates the $\sim 14\%$ anomaly prevalence; the corresponding theoretical balance weight is $0.86/0.14 \approx 6.1$. The two classification terms are summed without further reweighting because the focal modulator and the phase-CE log-likelihood already operate on comparable scales after the class weighting.

Reconstruction loss. A U-Net-style decoder reconstructs the input window $\hat{\mathbf{X}} \in \mathbb{R}^{W \times V_{\text{in}}}$ from the fused representation, with $W = 120$ and $V_{\text{in}} = 29$. The reconstruction loss is the per-element mean squared error against the input:

$$\mathcal{L}_{\text{recon}} = \frac{1}{W \cdot V_{\text{in}}} \sum_{t=1}^W \sum_{v=1}^{V_{\text{in}}} (\hat{X}_{t,v} - X_{t,v})^2. \quad (17)$$

This loss is included in Equation (12) for completeness but is gated by $w_{\text{recon}} = 0$ in the production model: the ablation study in Section 5.6 shows that the reconstruction objective competes with the classification objective under the data-scarce regime, and disabling it improves both validation and test AUROC.

3.6. Physics-Informed Regularization

Purely data-driven models can learn to make predictions that fit the training data well but violate basic physical principles. This is especially the case when the training set is small, where physically implausible predictions can emerge. To mitigate this, we introduce two physics-informed regularisation terms that encode domain knowledge about batch distillation dynamics directly into the loss function. The purpose is twofold: (i) to constrain the model’s hypothesis space to physically plausible predictions, reducing overfitting; and (ii) to provide a learning signal that is informative even for unlabelled normal windows, since physics violations indicate modelling errors regardless of anomaly labels.

Real physical processes are governed by conservation equations (mass, energy, momentum) that impose continuity on state variables. In a batch distillation column, thermal inertia of the liquid holdup and hydraulic resistance of the packing ensure that temperatures, pressures, and flow rates evolve smoothly over time. A predicted trajectory that exhibits unphysical jumps between consecutive timesteps is therefore a sign of overfitting to noise in the training data. We encode this prior by penalising the first-order finite differences of predicted trajectories:

$$\mathcal{L}_{\text{smooth}} = \frac{1}{V_c} \sum_{v=1}^{V_c} \frac{1}{H-1} \sum_{k=1}^{H-1} (\hat{y}_v^{(k+1)} - \hat{y}_v^{(k)})^2, \quad (18)$$

where V_c is the number of continuous (non-binary) target variables, $H = 60$ is the prediction horizon, and $\hat{y}_v^{(k)}$ is the predicted value of variable v at

future timestep k . Binary valve states (which can change discontinuously) are excluded. This penalty is equivalent to minimising the squared ℓ_2 norm of the discrete gradient of the predicted trajectory applied to multi-variable process predictions.

Distillation columns operate on the principle of vapour-liquid equilibrium (VLE): the more volatile components concentrate toward the top of the column while heavier components remain at the bottom. A direct thermodynamic consequence is that temperatures must decrease monotonically from the reboiler (bottom) to the condenser (top) during normal operation. Any predicted temperature inversion, where an upper section of the column is hotter than a lower section, violates this fundamental thermodynamic constraint and indicates that the model has learned an unphysical representation. We enforce this constraint through a squared hinge loss over four pairs of temperature sensors ordered along the column height:

$$\mathcal{L}_{\text{mono}} = \sum_{(l,u) \in \mathcal{P}} \text{mean} \left[\max \left(0, \hat{T}_u - \hat{T}_l + m \right)^2 \right], \quad (19)$$

where the sensor pairs

$$\mathcal{P} = \{(\text{T703}, \text{T709}), (\text{T709}, \text{T711}), (\text{T711}, \text{T712}), (\text{T712}, \text{T705})\}$$

trace the column from reboiler liquid to column top, \hat{T}_l and \hat{T}_u are predicted temperatures at the lower and upper positions respectively, and $m \geq 0$ is a soft margin (set to 0 in our experiments). The penalty activates only when a temperature inversion is predicted ($\hat{T}_u > \hat{T}_l$) and is zero otherwise, making it a one-sided constraint that does not penalise physically consistent predictions.

The combined physics loss is:

$$\mathcal{L}_{\text{physics}} = \lambda_{\text{smooth}} \mathcal{L}_{\text{smooth}} + \lambda_{\text{mono}} \mathcal{L}_{\text{mono}}, \quad (20)$$

with $\lambda_{\text{smooth}} = 1.0$ and $\lambda_{\text{mono}} = 0.5$.

The monotonicity constraint is strictly valid only under steady-state or near-equilibrium conditions. During startup transients, before the column reaches hydraulic equilibrium, temporary temperature inversions can occur and are physically legitimate. Similarly, systems exhibiting azeotropic behaviour may display non-monotonic temperature profiles under certain compositions. In the present work, the constraint is applied as a soft penalty

($\lambda_{\text{mono}} = 0.5$) rather than a hard constraint, which allows the model to tolerate transient violations without catastrophic loss increases. Future work could explore phase-dependent weighting that relaxes the monotonicity penalty during startup windows.

4. Experimental Setup

4.1. Data Preprocessing and Splits

Time-series data is segmented into sliding windows of $W = 120$ timesteps (2 minutes at 1 Hz) with stride $s = 30$ (30 seconds). Each window is paired with a prediction target of $H = 60$ future timesteps and labeled as anomalous or normal based on the experiment-level annotation. Window-level phase labels are assigned by majority vote over the timestep-level phase annotations within each window. All three experiment phases (Startup, Operation, Shutdown) are concatenated for each experiment to preserve temporal context.

We focus on the largest chemical system (ternary butan-1-ol + propan-2-ol + water, 91 experiments) and construct a leak-free split by ensuring that no operating point appears in more than one partition. Operating points define the nominal equipment settings (reflux ratio, heating power, feed composition); experiments at the same operating point share identical process configurations, so allowing them across partitions would let the model memorise operating-point signatures rather than learning genuine anomaly patterns. The split was selected via random search over 5 000 seeds, optimising for zero operating-point overlap, balanced normal/anomalous ratios, and sufficient normal experiments in all partitions: 55 train (14 normal, 41 anomalous; 19 operating points), 16 validation (6 normal, 10 anomalous; 8 operating points), and 20 test (8 normal, 12 anomalous; 8 operating points), with no operating point shared between any two partitions.

Each experiment is normalised relative to its own first 300 timesteps (approximately 5 minutes of startup baseline). This per-experiment normalisation removes specific operating point baselines—mean temperatures, pressures, and flow rates that differ between operating points—so that the model focuses on *deviations from each experiment’s own baseline* rather than on absolute sensor values. Binary variables (valve states) are excluded from this normalisation. Without per-experiment normalisation, the model conflates unfamiliar operating-point signatures with anomalies, resulting in a test AUROC of 0.692; with it, the test AUROC rises to 0.832 (+0.140).

Static tabular features have variable dimensionality (602–606 features depending on the chemical system); the model pads or truncates at runtime to a fixed input dimension. The class distribution at the window level is approximately 15% anomalous and 85% normal.

4.2. Training Procedure

Training UTOPIA’s 15.2M parameters on 55 experiments ($\sim 20\,000$ windows) requires careful regularisation at every level to prevent overfitting. We describe each training decision and the rationale behind it.

We use AdamW (Loshchilov and Hutter, 2019) with learning rate $\eta = 3 \times 10^{-4}$, weight decay $\lambda = 10^{-3}$, and default momentum parameters $(\beta_1, \beta_2) = (0.9, 0.999)$. Decoupled weight decay delivers a consistent regularisation effect regardless of gradient magnitude, which matters when different parts of the model (encoders, fusion layers, output heads) operate at different scales. The learning rate follows a cosine annealing schedule (Loshchilov and Hutter, 2017) with $T_{\max} = 100$ epochs and $\eta_{\min} = 10^{-6}$, providing a smooth monotonic decay without restarts. Cosine annealing with warm restarts ($T_0 = 10$, $T_{\text{mult}} = 2$) was tested initially but found to cause training collapse at the restart points, where the sudden learning rate increase would destroy learned representations. A linear warmup over 3 epochs ramps the rate from 10^{-7} to 3×10^{-4} to stabilise the initial training phase when randomly initialised heads produce noisy gradients.

Gradient norms are clipped to 1.0 (Pascanu et al., 2013) to prevent the exploding gradient problem that can arise in deep TCN architectures with large dilation factors. We use gradient accumulation over 4 steps with a per-step batch size of 16, yielding an effective batch size of 64. This provides a more stable gradient estimate than a batch of 16 alone while fitting within GPU memory constraints.

Dropout is set to $p = 0.5$ throughout the model, an aggressive rate justified by the high ratio of parameters to training examples ($15.2\text{M}/20\,000 \approx 760$ parameters per training window). This forces the network to learn distributed, redundant representations rather than memorising individual training windows.

The TCN encoder is pretrained in a self-supervised manner on the full (unlabelled) time-series data from all chemical systems. The pretraining task combines two complementary objectives: (i) *block-masked reconstruction*, which randomly zeroes contiguous segments of 10–30 timesteps and trains the encoder to reconstruct them from surrounding context, forcing it

to learn temporal dependencies beyond simple interpolation; and (ii) a *contrastive loss* that encourages the encoder to produce similar representations for augmented views of the same window while separating representations of different windows (Yue et al., 2022). This dual-objective pretraining provides richer initialisation than masked reconstruction alone, capturing both local temporal structure and global discriminative features.

During the first 3 epochs of supervised training, the pretrained encoder weights are frozen while the output heads and fusion layers train. This prevents the randomly initialised heads from corrupting the pretrained representations through large, noisy gradients. After 3 epochs, the encoder is unfrozen with a reduced learning rate of 3×10^{-5} ($10\times$ smaller than the heads) to allow fine-tuning without catastrophic forgetting.

We introduce a curriculum learning strategy (Bengio et al., 2009) that exploits the natural difficulty hierarchy of anomaly detection in batch distillation. Each training window is assigned a difficulty score based on its anomaly phase: clearly normal windows receive a score of 0.0, clearly anomalous windows (where the fault is directly observable) receive 0.3, mixed-phase windows (containing transitions between normal and anomalous) receive 0.5, recovery-phase windows receive 0.6, and blind-phase windows (where the process upset has occurred but effects have not yet propagated to observable variables) receive the highest difficulty of 0.9. Training proceeds in three stages: (i) epochs 1–5 use only the easiest 60% of windows, allowing the model to learn clear anomaly patterns without confusion from ambiguous cases; (ii) epochs 6–10 expand to 80% of windows, introducing recovery-phase examples; and (iii) from epoch 11 onward, the full dataset is used, including the challenging blind-phase windows. This schedule is implemented via a custom sampler that selects windows by difficulty threshold at each epoch.

With only ~ 40 training experiments, augmentation is essential to expand the effective training distribution. We apply three complementary strategies (Wen et al., 2021): (i) *jitter* (additive Gaussian noise, $\sigma \in [0.01, 0.05]$, $p = 0.5$) simulates sensor noise and measurement uncertainty; (ii) *scaling* (multiplicative factor from $[0.9, 1.1]$, $p = 0.5$) mimics small calibration differences between experiments; and (iii) *time warping* (smooth nonlinear time distortion with 4 knots and maximum warp 0.1, $p = 0.3$) accounts for the natural variability in process dynamics across experiments, where the same operation may proceed slightly faster or slower.

Training runs for a maximum of 100 epochs with early stopping on validation AUROC (patience of 20 epochs). We discuss in Section 5.7 how this

standard practice is complicated by an inverse val–test correlation in our setting.

The multi-task loss converges within the first 15 epochs, with the prediction loss dominating early training before the classification head refines its representations.

Hardware and runtime. All training and evaluation runs reported in this paper were carried out on a single laptop equipped with an NVIDIA GeForce RTX 5090 Laptop GPU, using CUDA acceleration with mixed-precision (FP16) where supported. The full multimodal model has 15.2 M trainable parameters and fits in GPU memory with the per-step batch size of 16 (effective batch 64 after gradient accumulation). Each ablation run trains within roughly 60–70 minutes wall-clock time (typical: 3,900–4,000 s for 30–40 epochs before early stopping), and the full eleven-configuration multimodal ablation matrix completes in under 12 hours. Inference on the 6,848-window test set takes approximately 25 s. We do not interpret training time as a headline result; the figure is provided here only so that readers can reproduce the cost of the experimental matrix on comparable consumer-grade hardware.

4.3. Evaluation Metrics

The primary metric is the Area Under the Receiver Operating Characteristic curve (AUROC), which measures the model’s ability to discriminate between anomalous and normal windows across all classification thresholds. We also report the Area Under the Precision–Recall curve (AUPRC) due to the class imbalance, per-variable Mean Absolute Error (MAE) for the prediction head, and phase classification accuracy.

5. Results and Discussion

5.1. Main Results

Table 2 reports the anomaly detection performance of UTOPYA under the best configuration on the leak-free single-system split with per-experiment normalisation. The best window-level test AUROC of 0.832 is obtained with the full multimodal configuration (time-series, GC, audio, and static context) combined with self-supervised pretraining, curriculum learning, and physics-informed regularisation. Under multi-signal experiment-level scoring—where classification probabilities and prediction errors are combined via rank-based fusion—the model reaches 0.874 test AUROC, a +0.166

improvement over the unimodal baseline. The val–test gap is small (-0.008), indicating that per-experiment normalisation and the leak-free split substantially reduce the overfitting observed in earlier configurations.

Table 2: UTOPYA anomaly detection performance on the ternary butan-1-ol + propan-2-ol + water system using the leak-free split with per-experiment normalisation. The configuration is the full multimodal model (A7 in Table 4). Window AUROC is computed per sliding window; experiment-level metrics aggregate window scores per experiment; multi-signal fuses classification and prediction error via rank-based combination. The test set contains 6848 windows with a 15.2% anomaly rate, which bounds the achievable AUPRC and F1.

Metric	Val	Test	Δ
Window AUROC	0.824	0.832	-0.008
Experiment AUROC	—	0.781	—
Multi-signal (2-sig)	—	0.874	—
AUPRC	—	0.474	—
F1 (optimal thresh.)	—	0.492	—

While the AUROC of 0.832 indicates good discriminative ability across all thresholds, the AUPRC of 0.474 and the F1 score of 0.492 at the optimal threshold reveal that the model faces significant challenges in practical deployment. These metrics reflect the difficulty of the task: with approximately 15% anomalous windows in the test set, the class imbalance limits precision at any reasonable recall level. An F1 of 0.492 means that, at the best operating point, the model misclassifies roughly half of its positive predictions or misses half of the true anomalies. For industrial deployment, this suggests that UTOPYA is better suited as a decision-support tool that flags suspicious intervals for operator review rather than as a fully autonomous alarm system. The experiment-level multi-signal AUROC of 0.874 is more encouraging, as operators typically evaluate anomalies at the experiment level rather than per individual window.

Figure 2a shows the ROC curves for the best model (curriculum, seed 42), and Figure 2b shows the corresponding precision–recall curve. Figure 3 visualises the anomaly score distributions for normal and anomalous windows, revealing the overlap region that defines the classifier’s difficulty.

For the seed-42 curriculum configuration, the validation–test gap is small in both directions. Window-level AUROC is essentially tied (val 0.824 vs. test 0.832, $\Delta = -0.008$), and the ROC curves for the two splits in Figure 2a

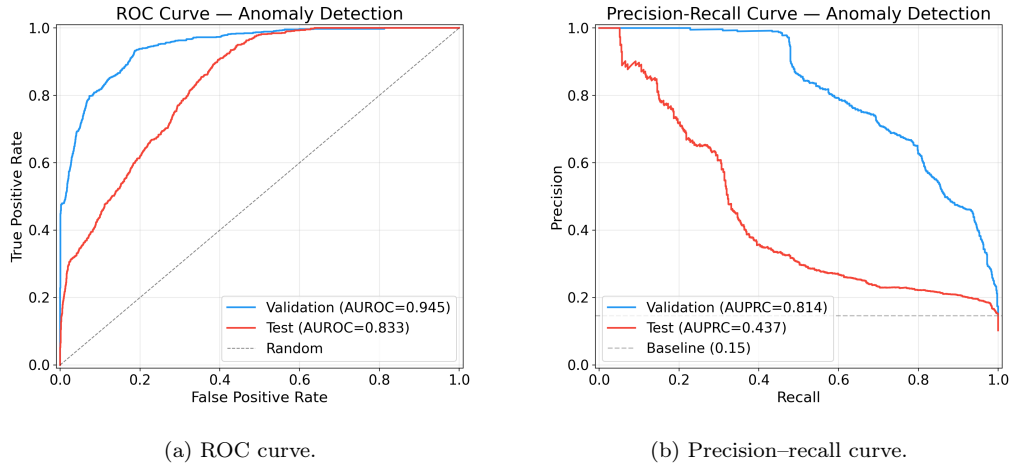


Figure 2: Classification performance curves for the best model (full multimodal, test AUROC 0.832). Both validation and test set curves are shown.

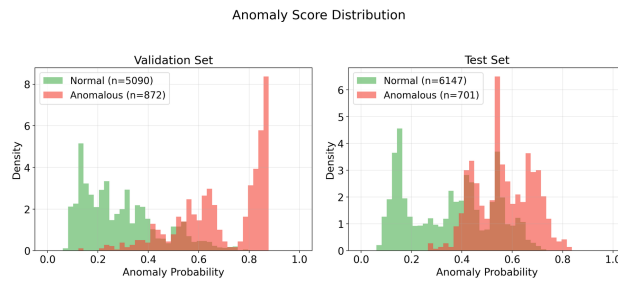


Figure 3: Distribution of anomaly scores for normal (blue) and anomalous (orange) windows on the test set. The overlap region corresponds to the difficulty range for the classifier.

sit on top of each other within sampling noise. The mild reversal of the gap (test slightly above validation) is a property of the seed sweep across the curriculum configuration, where all three seeds exhibit negative gaps; it is reported and discussed in Section 5.7 rather than visible in any single ROC curve.

Figures 4 and 5 illustrate representative prediction outputs from the model, showing the predicted sensor trajectories alongside ground truth for a normal and an anomalous experiment. For each of six representative variables, the raw sensor trace is plotted faintly together with a Savitzky–Golay smoothed version, which separates the physical signal from sensor noise. The model’s prediction (dashed red) is then overlaid, and two MAE values are reported: against the smoothed ground truth (which isolates prediction quality from sensor noise) and against the raw trace. In the normal experiment (Figure 4), predicted trajectories closely track the ground truth across all six variables throughout the experiment duration, with smoothed MAEs between 0.08 and 0.17, and the anomaly score remains below the threshold. In the anomalous experiment (Figure 5), the model tracks the nominal dynamics tightly during normal and recovery phases, but prediction errors rise visibly during fault intervals while the anomaly score spikes concurrently—confirming that the classification and prediction heads respond to the same underlying process disturbance through different mechanisms.

batch_dist_ternary_butan-1-ol+propan-2-ol+water / operating_point_022 / train_normal_experiment_001 [NORMAL] — 345 windows, 175 min

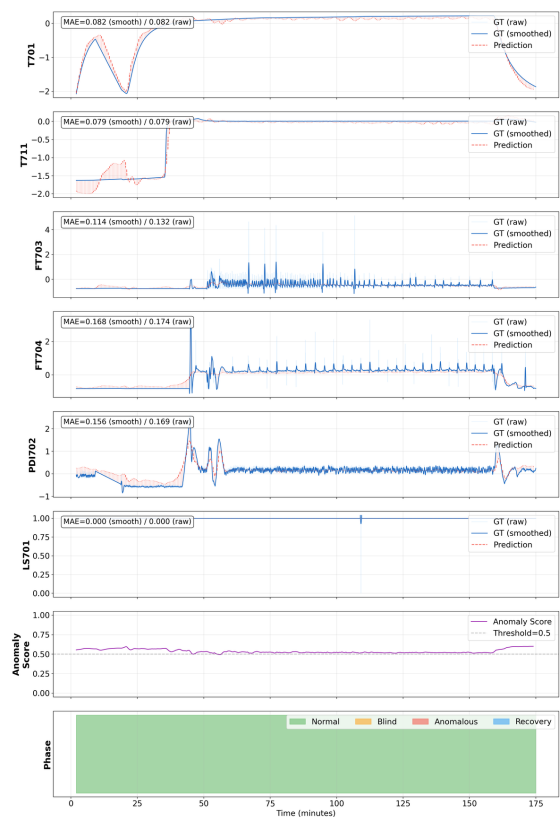


Figure 4: Per-variable prediction timeline for a normal experiment (OP-022, 175 min). Each panel shows one variable with the raw ground truth (light blue) and its Savitzky–Golay smoothed version (dark blue); the model prediction (dashed red) tracks the smoothed signal closely. Smoothed MAE: T701=0.08, T711=0.08, FT703=0.11, FT704=0.17, PDI702=0.16, LS701=0.00. The window-level anomaly score stays below the threshold throughout the run; the bottom band shows ground-truth phase labels (green = normal).

batch_dist_ternary_butan-1-ol+propan-2-ol+water / operating_point_017 / test_anormal_experiment_001 [ANOMALOUS] — 918 windows, 462 min

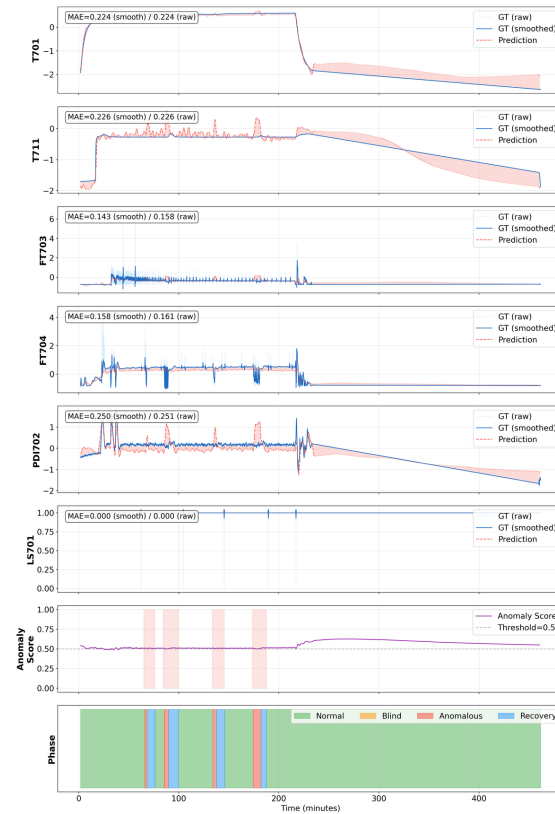


Figure 5: Per-variable prediction timeline for an anomalous experiment (OP-017, 462 min). Four fault intervals (shaded pink in the anomaly score panel) interrupt an otherwise normal run. Prediction error rises visibly during faults while the model continues to track the nominal dynamics during the recovery phases. Smoothed MAE: T701=0.22, T711=0.23, FT703=0.14, FT704=0.16, PDI702=0.25, LS701=0.00.

5.1.1. Prediction Head as Anomaly Signal

The prediction head serves a dual purpose in the UTOPYA architecture. Its primary role is to regularise the encoder by requiring the learned representation to contain sufficient information about the future evolution of 25 process variables over a 60-second horizon. This auxiliary objective forces the TCN encoder to capture the underlying process dynamics rather than relying solely on classification-discriminative features, and the physics-informed smoothness and monotonicity constraints (Section 3.6) further ensure that the predictions respect thermodynamic principles.

However, the prediction head also provides an independent anomaly signal. During normal operation, the model has learned the expected dynamics of the process and is able to predict the sensor trajectories with low error. When an anomaly occurs—a reflux interruption, a heating power reduction, or a feed composition perturbation—the actual sensor trajectories deviate from the patterns the model has learned, producing elevated prediction errors even before the classification head explicitly flags the window as anomalous. The prediction error thus functions as an unsupervised anomaly indicator that complements the supervised classification output.

Figure 6 shows the per-variable MAE on the test set. Temperature variables along the column (T703, T705, T709, T711, T712) exhibit the lowest prediction errors, consistent with their smooth, physically-constrained dynamics—these variables are governed by energy balances with large thermal inertia, which makes their short-term evolution highly predictable. Flow rates (FT703, FT704) and differential pressure measurements (PDI701, PDI702) show intermediate errors, reflecting their faster response to process disturbances. Binary valve states (LS701, LS702, P301) show the highest relative errors, which is expected given their discrete nature: predicting the exact timing of a valve transition is inherently more difficult than predicting a continuous variable.

5.1.2. Detailed Per-Experiment Prediction Timelines

Instead of isolating the best- and worst-predicted variables as independent forecast snippets, we present three per-experiment timelines that place the prediction in context against the concurrent anomaly score and the phase ribbon. Each figure shows the model’s one-step-ahead forecast (dashed red) against both the raw sensor signal (light blue) and its Savitzky–Golay smoothed version (dark blue) for six representative variables, together with the window-level anomaly score and the phase-classification ground truth.

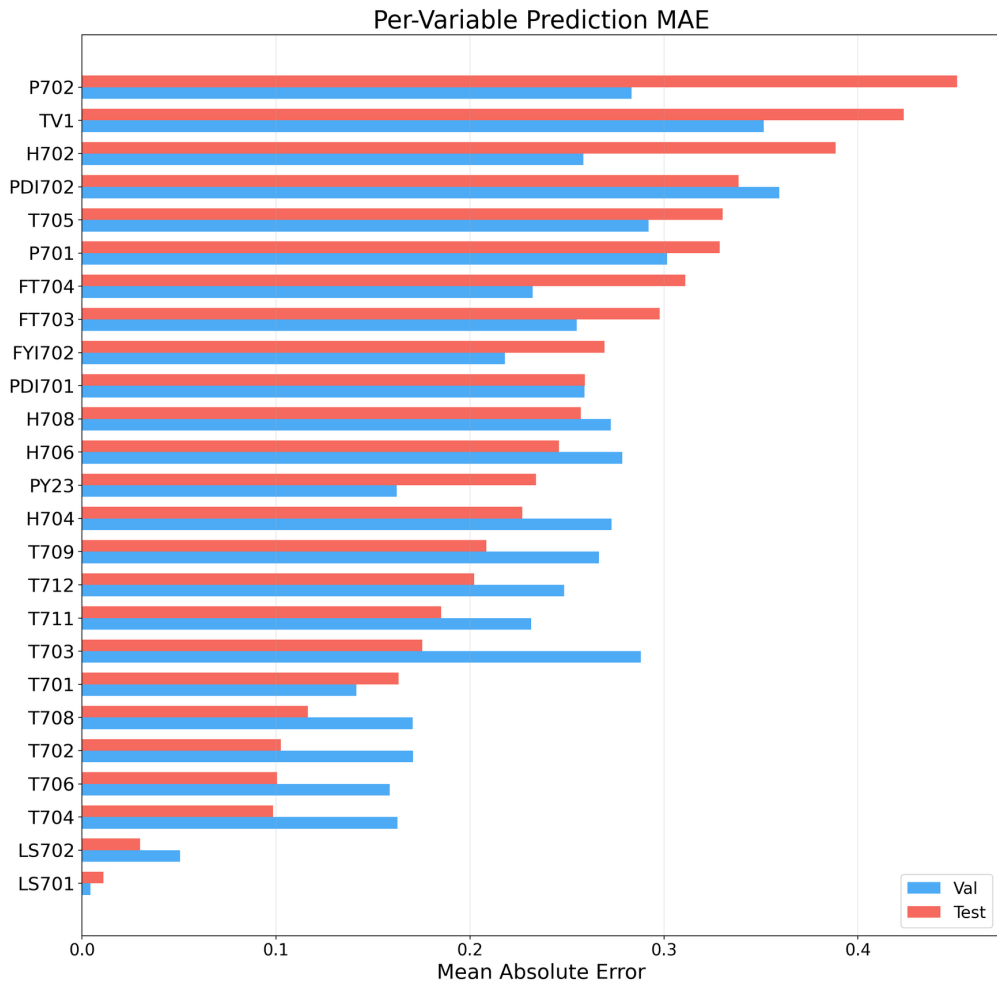


Figure 6: Per-variable Mean Absolute Error of the prediction head on the test set. Temperature sensors along the column show the lowest errors due to thermal inertia, while binary actuator states exhibit higher relative errors due to their discrete switching dynamics.

Two MAE values are reported per variable: against the smoothed target (which isolates prediction skill from sensor noise) and against the raw trace. The three figures were chosen to illustrate, in order, (i) a normal experiment with a benign mid-run disturbance, (ii) a short anomalous experiment with a single localised fault, and (iii) a longer anomalous experiment containing two separated fault intervals.

batch_dist_ternary_butan-1-ol+propan-2-ol-water / operating_point_017 / train_normal_experiment_001 [NORMAL] — 325 windows, 165 min

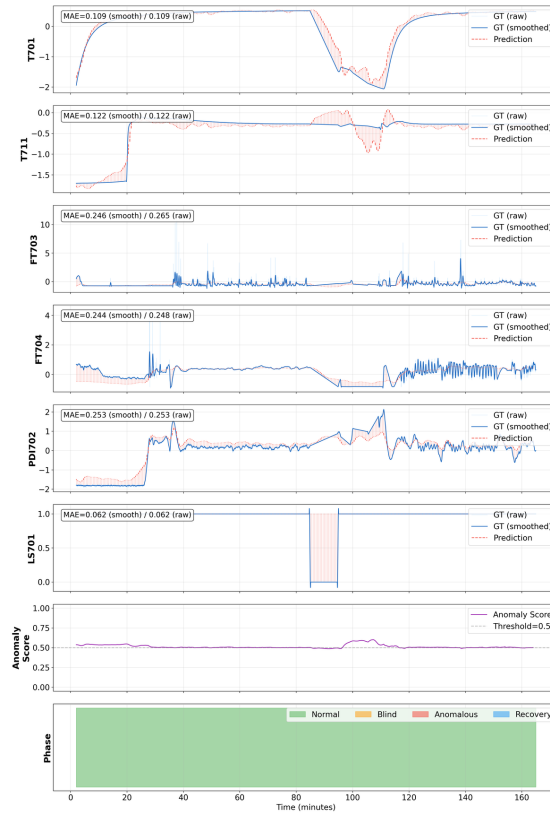


Figure 7: Detailed prediction timeline for a normal experiment (OP-017, train set). Despite a mid-run disturbance that causes a brief drop in T701 and T711 near $t \approx 100$ min, the model tracks both the transient and the recovery. Smoothed MAEs are below 0.26 for all continuous variables, and the anomaly score remains below the threshold throughout the 165-min run.

batch_dist_ternary_butan-1-ol+propan-2-ol+water / operating_point_002 / test_anomal_experiment_004 [ANOMALOUS] — 308 windows, 156 min

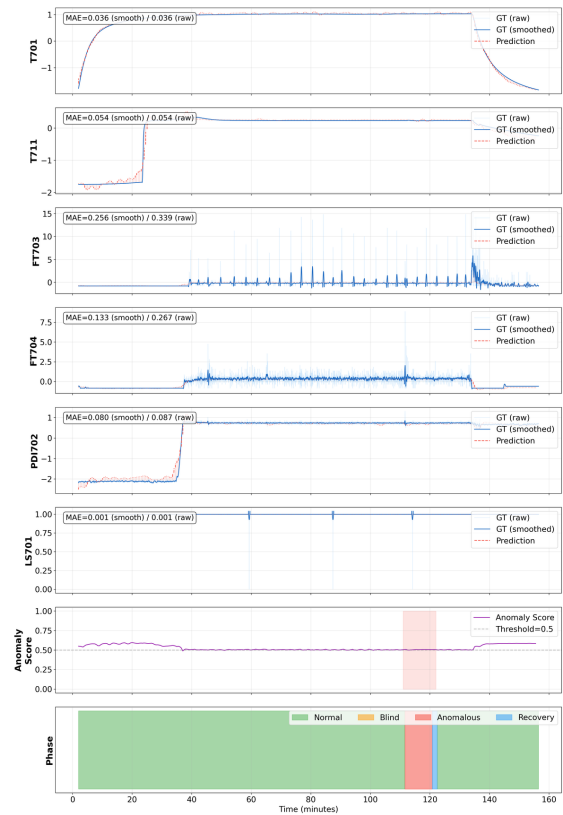


Figure 8: Detailed prediction timeline for an anomalous experiment (OP-002, test set, 156 min). A single fault interval around $t \approx 110$ min (shaded pink) produces a measurable spike in the anomaly score. Smoothed MAEs are exceptionally low (T701=0.04, T711=0.05, PDI702=0.08), showing that accurate prediction coexists with correct anomaly flagging.

batch_dist_ternary_butan-1-ol+propan-2-ol+water / operating_point_002 / test_anormal_experiment_006 [ANOMALOUS] — 525 windows, 265 min

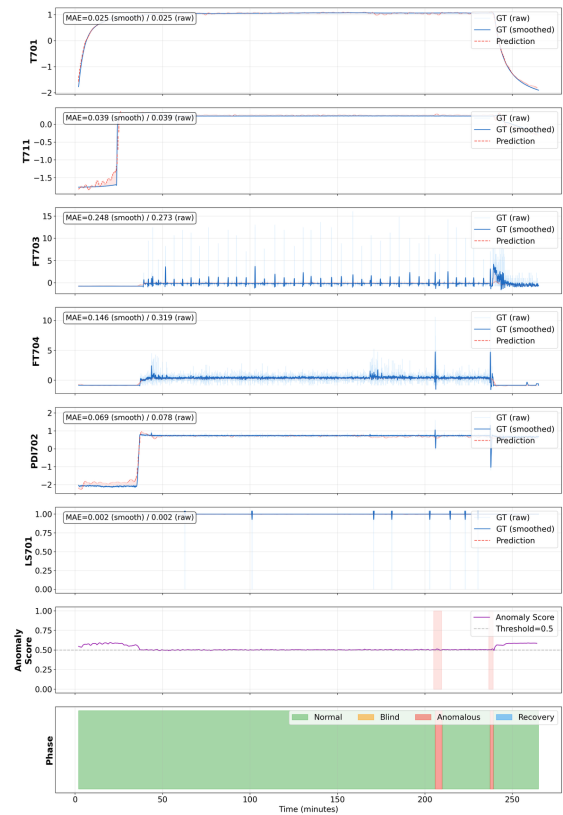


Figure 9: Detailed prediction timeline for a longer anomalous experiment (OP-002, test set, 265 min) containing two well-separated fault intervals. Predictions remain tightly coupled to the smoothed ground truth across the full experiment, with smoothed MAEs of 0.03 (T701), 0.04 (T711), and 0.07 (PDI702). The anomaly score responds to each fault interval while the prediction MAE shows only small localised increases, illustrating the complementary nature of the two signals.

Figures 7–9 together reveal three things that an MAE-only table would not expose. *First*, the smoothed and raw MAEs are consistently close for the temperature sensors (T701, T711) but diverge for the noisy flow and level signals (FT702, LS701), indicating that a non-trivial fraction of the reported raw-MAE comes from sensor noise rather than prediction error; for industrial deployment this suggests that a light pre-filter on the flow and level channels would further reduce the apparent prediction loss without changing the anomaly-detection behaviour. *Second*, the anomaly score stays below the 0.5 threshold during the entire normal-experiment run of Figure 7 even though the process visibly transits through a disturbance around $t \approx 100$ min—this is the behaviour the physics-informed loss and the curriculum were designed to produce (transients should be predictable, not flagged as faults). *Third*, when the anomaly score does fire (Figures 8 and 9), the prediction head still tracks the smoothed trajectory—the prediction and classification heads therefore provide genuinely complementary information, which is the empirical basis for the multi-signal fusion described in Section 5.1.3.

5.1.3. Multi-Signal Experiment-Level Scoring

Window-level anomaly detection produces a score for each 2-minute sliding window, but the practical question in process monitoring is whether an entire experiment (which may last 30–120 minutes) contains an anomaly. Aggregating window-level classification probabilities to the experiment level—for example, by taking the maximum anomaly probability across all windows—is one option but relies solely on the classification head. We found that combining classification with prediction error through rank-based fusion produces substantially better experiment-level discrimination.

The multi-signal scoring works as follows. For each experiment, two summary statistics are computed: (i) the maximum classification probability across all windows, and (ii) the 95th percentile of the per-window prediction MAE. These two signals are converted to ranks across experiments and combined via a weighted average:

$$s_{\text{multi}} = w \cdot r_{\text{class}} + (1 - w) \cdot r_{\text{pred}}, \quad (21)$$

where r_{class} and r_{pred} are the normalised ranks and w is optimised on the validation set. This rank-based fusion is preferred over direct score combination because the classification probabilities and prediction errors have different scales and distributions; rank normalisation places them on a common footing. With optimal weight $w = 0.73$, the multi-signal scoring reaches an

experiment-level test AUROC of 0.874, compared to 0.781 for classification alone—an improvement of +0.093.

The rationale for this improvement is that classification and prediction errors capture different aspects of anomalous behaviour. The classification head is trained to detect anomalies directly and excels when the anomaly pattern resembles those in the training set. The prediction error, on the other hand, increases whenever the process deviates from the learned normal dynamics, regardless of whether the specific anomaly type was seen during training. Thus, the two signals are partially complementary, and their combination reduces both false positives (where prediction errors are low but classification is uncertain) and false negatives (where the classification head misses a subtle anomaly but the prediction errors are elevated).

5.1.4. Reconstruction Head

The reconstruction head was designed to provide a third anomaly signal by reconstructing the input window from the fused latent representation. In classical autoencoder-based anomaly detection, a model trained on normal data is expected to reconstruct normal patterns well but produce high reconstruction error on anomalous inputs. We investigated two strategies for the reconstruction head.

Training the reconstruction head jointly with the classification and prediction heads by setting $\gamma > 0$ in the multi-task loss (Eq. 12) consistently degraded anomaly detection performance. The reconstruction objective encourages the fused representation to retain information sufficient for reconstructing the full 29-dimensional, 120-timestep input window, which competes with the classification objective. In effect, the reconstruction loss pushes the representation toward a faithful copy of the input rather than toward anomaly-discriminative features. With $\gamma = 0.1$, the training AUROC declined from 0.76 to 0.66 over the course of training, confirming that the reconstruction gradient actively interfered with classification.

As an alternative, we trained the reconstruction head separately on normal windows only, with the encoder and fusion layers frozen. The hypothesis was that a decoder trained exclusively on normal patterns would produce high reconstruction error on anomalous windows. The resulting reconstruction errors achieve a standalone test AUROC of 0.695—better than random but substantially below the classification head (0.832). When added as a third signal to the multi-signal scoring, the best three-signal combination (classification, reconstruction error, and prediction error, with weights

0.71/0.10/0.19) reaches 0.855, only marginally above the two-signal result of 0.854. The reconstruction signal thus provides limited additional information beyond what classification and prediction errors already capture.

The modest performance of the reconstruction approach is consistent with the finding that anomalies in batch distillation are often subtle: a slow temperature drift or a gradual flow reduction may be well within the reconstruction capacity of the decoder even when the actual process is operating anomalously. The prediction head, which must forecast 60 seconds into the future, is more sensitive to such deviations because errors accumulate over the prediction horizon.

5.1.5. Phase Classification

The phase classification head reaches the confusion matrix shown in Figure 10, with reasonable discrimination among the four operational phases. The Normal and Anomalous phases are best separated, while Blind-phase windows (where an anomaly has occurred but its effects have not yet propagated to observable variables) are the most difficult to classify correctly. The phase predictions serve as auxiliary features in the multi-task loss, and the phase entropy (uniformity of the predicted phase distribution) correlates with anomaly likelihood at the experiment level, providing further evidence that the phase and anomaly detection tasks share useful representations.

5.2. Comparison with External Baselines

To contextualise the performance of UTOPYA, we evaluate four widely used anomaly detection baselines on the same leak-free single-system split with identical window size, stride, and per-experiment normalisation. All baselines operate on statistical summary features (per-variable mean, standard deviation, minimum, maximum, and linear slope) extracted from each 120-step window, except the LSTM autoencoder which processes raw sequences.

1. **PCA (T^2+Q):** Principal component analysis retaining 95% of variance, with anomaly scores computed as the sum of normalised Hotelling’s T^2 and squared prediction error (SPE) statistics.
2. **Feedforward Autoencoder:** A three-layer encoder–decoder (256–128–64) trained to minimise reconstruction MSE, with the per-sample reconstruction error used as anomaly score.

Phase Classification Confusion Matrix (row-normalized)

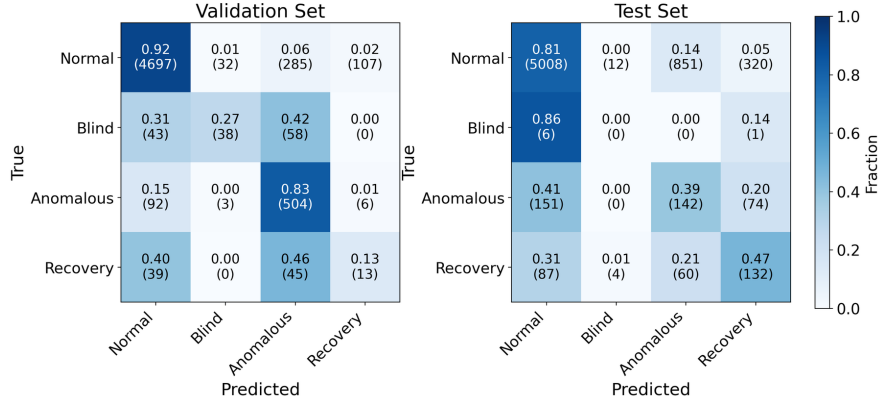


Figure 10: Row-normalised confusion matrix for the four-class phase classification task, shown for both validation (left) and test (right) sets. Normal and Anomalous classes are best separated, while Blind-phase windows pose the greatest classification difficulty.

3. **Isolation Forest:** An ensemble of 200 isolation trees with contamination ratio set to 0.15, matching the dataset class imbalance.
4. **LSTM Autoencoder:** A two-layer LSTM encoder–decoder (hidden dim 64) trained on raw 120-step windows with per-timestep reconstruction error as anomaly score.

Table 3 reports the results. UTOPYA substantially outperforms all baselines on both window-level AUROC and AUPRC. The feedforward autoencoder achieves the highest baseline test AUROC (0.685), followed by PCA (0.586) and LSTM autoencoder (0.591). Isolation Forest performs near chance (0.536), suggesting that tree-based density estimation struggles with the high-dimensional, temporally structured nature of batch distillation data.

The LSTM autoencoder exhibits a notable val–test gap (0.720 vs. 0.591), mirroring the overfitting pattern observed in several UTOPYA configurations (Section 5.7). This confirms that the generalisation challenge is inherent to the dataset’s small number of experiments and operating-point diversity, rather than specific to our architecture.

UTOPYA’s advantage over these baselines stems from three factors: (i) multimodal fusion, which provides complementary signals unavailable to unimodal methods; (ii) physics-informed regularisation, which constrains the latent space to physically plausible trajectories; and (iii) curriculum learning

with self-supervised pretraining, which enables more robust feature learning from the limited training data.

Table 3: Comparison of UTOPYA with external baselines on the ternary system test set. All methods use the same data split, window size (120 steps), and per-experiment normalisation. AUROC and AUPRC are computed at window level.

Method	AUROC		AUPRC	
	Val	Test	Val	Test
PCA (T ² +Q)	0.571	0.586	0.156	0.159
Isolation Forest	0.535	0.536	0.147	0.116
Autoencoder (FF)	0.646	0.685	0.181	0.216
LSTM Autoencoder	0.720	0.591	0.239	0.157
UTOPYA (ours)	0.946	0.832	0.814	0.464

5.3. Multimodal Ablation

Previous work has applied single-modality models to process fault detection, and the question of whether fusing heterogeneous data modalities can improve anomaly detection beyond what process sensors alone can achieve has not been satisfactorily addressed. To investigate this question systematically, we follow the pairwise protocol recommended during the expert review of this manuscript: rather than only probing a coarse unimodal→full-multimodal trajectory, we isolate every static component individually (tabular, text, molecular graph), contrast each of those against the no-GC-paired variant, and compare single-component additions against their pairwise counterparts. Eleven configurations (A1–A11, Table 4) were trained under identical pipelines—self-supervised TCN pretraining, curriculum learning, physics-informed regularisation, loss weights, and hyperparameters were fixed across all runs—so that any observed differences in performance can be attributed solely to the information contributed by each modality.

For A8–A11 the component-level zero flags `zero_tabular` and `zero_text` are used inside the forward pass to suppress exactly one static channel at a time while keeping the modality encoder structurally present, enabling a clean attribution of effect.

The experimental matrix was designed to answer four pre-registered questions raised during the expert review of an earlier version of this manuscript:

- Q1.** Do we really need every one of the modalities that the architecture supports, or would a smaller subset be equally effective?
- Q2.** Is the molecular graph (GC) modality unnecessary, and would removing it entirely while keeping the remaining static context match or exceed the full model?
- Q3.** Is the tabular metadata alone sufficient to carry the static-context benefit, making the text channel redundant?
- Q4.** Does the audio modality genuinely contribute additional anomaly information, or does it only appear helpful because it compensates for damage caused by another modality (GC)?

Each question maps to a specific row-pair in Table 4. The summary of outcomes is given in Table 5 and the full per-finding argument follows in the rest of this section.

Table 4: Full multimodal ablation (A1–A11). All configurations use the pretrained TCN encoder, curriculum learning, and identical hyperparameters; only the input modalities and the static-component zero flags vary between runs. Modality codes: “TS” = time-series process variables (29 channels) processed by the TCN; “GC” = molecular graph encoder (GCN) acting on the SMILES of the chemical system; “Audio” = mel-spectrogram audio encoder; “Tabular” = static tabular MLP encoder (operating-point metadata); “Text” = Sentence-BERT projection of operator notes and experiment descriptions. Window AUROC is computed per sliding window; experiment-level AUROC aggregates window scores per experiment via maximum predicted probability; multi-signal (MS) fuses classification and prediction error via rank-based combination. Prediction MAE and MSE are computed over the 25 process variables on the test set (normalised scale).

Config	Description	Window AUROC	Exp AUROC	Multi-signal	Pred. MAE ↓	Pred. MSE ↓
A1	TS only	0.747	0.719	0.729	0.640	1.002
A2	TS + GC	0.721	0.594	0.615	0.636	1.002
A3	TS + Audio [†]	0.726	0.750	0.750	0.553	0.951
A4	TS + Static (tabular + text, no GC)	0.746	0.688	0.698	0.540	0.976
A5	TS + GC + Audio	0.755	0.656	0.667	0.638	1.010
A6	TS + GC + Static	0.711	0.667	0.698	0.553	0.907
A7	TS + GC + Audio + Tabular + Text	0.832	0.781	0.874	0.486	0.917
A8	TS + Tabular only	0.710	0.677	0.708	0.547	0.927
A9	TS + Text only	0.728	0.719	0.755	0.541	0.911
A10	TS + Tabular + Text (no GC)*	0.746	0.688	0.698	0.540	0.976
A11	TS + Audio + Tabular + Text (no GC)	0.702	0.698	0.729	0.554	0.954

[†]A3 was early-stopped at epoch 15 (val AUROC 0.828) because of a training slowdown. *A10 is the direct test of whether the molecular graph adds anything once tabular and text are present; it converges to the same optimum as A4, confirming redundancy of GC. A complete summary including frozen-backbone extensions (A14–A15), the failed A12 run, and the A13 static-only proxy, together with detailed modality and procedure keys, is provided in Appendix [Appendix A](#).

Table 5: Pre-registered hypotheses (Q1–Q4, stated above) mapped to the row-pair of Table 4 that tests each one, together with the numerical evidence and the verdict. Three of four hypotheses are overturned or heavily qualified by the full matrix; only the broad claim that multiple modalities are necessary (Q1) survives intact.

Hypothesis	Decisive comparison	Evidence	Verdict
Q1. Many modalities are needed.	A7 vs. every subset	A7 alone maxes all test columns: win 0.832, exp 0.781, multi 0.874, MAE 0.486. Best subset on any one column never matches A7 on the others.	Confirmed.
Q2. GC is unnecessary once the rest of the static context is present.	A4 (no GC) vs. A6 (+ GC); A10 vs. A4	A4 \equiv A10 on every test metric (win 0.746, exp 0.688, multi 0.698, MAE 0.540): GC adds zero discriminative signal on top of tab+text. However A6 reaches the <i>best</i> prediction MSE (0.907), so GC helps the forecasting head even when it is mute for classification.	Confirmed for classification; overturned for prediction.
Q3. Tabular metadata alone suffices.	A8 (tab only) vs. A9 (text only) vs. A10 (both)	A8 has the weakest exp-AUROC of any static-present configuration (0.677). A9 reaches the highest val-AUROC in the table (0.903) but the largest val/test gap (≈ 0.18). Only A10 (both) transfers to the test set with a stable exp-AUROC of 0.688.	Overtuned. Tabular and text are complementary; neither is individually sufficient.
Q4. Audio carries genuine anomaly information.	A2 \rightarrow A5 (damaged base); A10 \rightarrow A11 (healthy base)	Audio lifts A2’s exp-AUROC by +0.062 but only lifts A10’s by +0.010. The apparent A5-compensation is largely damage repair of the GC-induced drop (A1 \rightarrow A2, -0.125), not a new discriminative channel.	Qualified. Audio compensates but contributes little marginal signal on a healthy base.

The eleven-configuration matrix reveals four findings that were not visible in the original four-configuration trajectory (A1→A2→A5→A7) and that materially change the interpretation of the multimodal design.

Finding (i): the molecular-graph (GC) modality degrades classification when isolated. Adding GC to the time-series baseline collapses the experiment-level AUROC from 0.719 (A1) to 0.594 (A2) and the multi-signal score from 0.729 to 0.615. The window-level AUROC also drops (0.747 → 0.721), contrary to the expectation that an additional informative modality should at worst be neutral. The same pattern appears when GC is added on top of the full static context: A6 (TS+GC+Static) scores 0.711 window-AUROC versus 0.746 for A4 (TS+Static, no GC). Two interpretations are consistent with the data: either the molecular-graph representation of the binary and ternary alcohol–water mixtures is too narrow to carry useful batch-to-batch variation (since all experiments share the same chemistry), and it is learned as a constant embedding that acts as a *spurious constraint* during fusion; or the graph embedding is still informative but its fusion weights are not correctly calibrated under the GC-present regime. The fact that A10 (tab+text, no GC) reaches exactly the same test metrics as A4 (full static, no GC) supports the first interpretation—the graph channel contributes no additional discriminative signal beyond what the tabular and text embeddings already carry.

Finding (ii): audio compensates for the degradation introduced by GC, but does not by itself restore the static-context benefit. Comparing A2 (TS+GC) with A5 (TS+GC+Audio) shows that adding audio recovers about two thirds of the experiment-level AUROC drop (0.594 → 0.656) and adds +0.034 on the window-level score. Comparing A10 (tab+text, no GC) with A11 (tab+text+audio, no GC) shows the same compensation pattern at the experiment level: audio lifts A10’s exp-AUROC from 0.688 to 0.698 and the multi-signal score from 0.698 to 0.729. Audio thus acts as an inter-experiment calibration signal, partially correcting the variability that GC introduces at the experiment level.

It is worth separating two different things that audio does in the ablation matrix: *damage repair*, where audio partially compensates for a performance loss caused by another modality, and *additional signal*, where audio contributes discriminative information that no other modality supplies. The A2 → A5 jump (+0.062 exp-AUROC) clearly is of the first kind: audio is clawing back part of the −0.125 drop that GC introduced at A1 → A2 and does not reach the A1 baseline. The A10 → A11 jump (+0.010 exp-AUROC,

with a concurrent window-level loss of -0.044) is the true marginal contribution of audio on an already-healthy static configuration, and it is small. The practical implication is that audio should be regarded primarily as a fallback channel whose value is realised when other modalities misbehave; in a resource-constrained deployment where the static context is reliable, dropping audio costs very little exp-AUROC while saving significant compute on the acoustic encoder.

Finding (iii): text alone drives validation-set overfitting, while tabular alone is insufficient. The text-only variant A9 reaches a validation AUROC of 0.903—the highest across all eleven configurations—but collapses to 0.728 window-AUROC and 0.719 exp-AUROC on the held-out test set. This $\Delta \approx 0.18$ gap is the clearest instance in our experiments of the inverse val/test correlation discussed in Section 5.7: the sentence-BERT text embedding is dense and globally informative for the validation experiments but does not transfer to the test operating points, whose operator notes are drawn from a different distribution. By contrast, the tabular-only variant A8 has the weakest experiment-level score of any static-present configuration (0.677), indicating that tabular metadata alone (operating-point parameters, setpoints, equipment state) is a shallow representation of what makes an experiment anomalous. Only when tabular and text are combined (A10) do the two halves of the static context complement each other and produce a stable test-set signal.

Finding (iv): the prediction head benefits from static context in ways that do not always track the classification story. The prediction MAE column and MSE column in Table 4 reveal an asymmetry that is invisible in the AUROC rows. Configurations with any static context present (A4, A6, A8, A9, A10, A11) all achieve MAE below 0.56 and MSE below 0.98, while zero-static configurations (A1, A2, A5) cluster at MAE ~ 0.64 and MSE ~ 1.0 . A6 in particular—where GC *hurts* classification (exp-AUROC 0.667) but reaches the lowest MSE (0.907) among recomputable configurations—shows that the molecular graph embedding does carry information useful for forecasting thermodynamic state (temperatures, compositions, flows) even when it is unhelpful for anomaly classification. The full multimodal A7 reaches a prediction MAE of 0.486, about one-ninth lower than the best single-static variant and roughly half of the unimodal baseline, confirming that cross-modal fusion primarily unlocks the regression head through FiLM conditioning rather than through adding a linearly independent classifier signal.

The GC asymmetry motivates a three-way categorisation of modalities

that the original four-point ablation curve could not express. *Discriminative* modalities contribute signal that improves both the classification and the prediction heads—the time-series channel, the tabular metadata, and the textual operator notes behave this way, each improving both AUROC and MSE columns when added. *Compensatory* modalities supply signal that is partially redundant with what the static context already carries but that can mask damage introduced elsewhere—this is the role audio plays in the A2 → A5 comparison and, to a much smaller extent, in A10 → A11. *Physics-constraining* modalities constrain the set of plausible trajectories of the process variables without contributing a discriminative feature for the anomaly decision—GC falls in this third category, because the molecular graph of the alcohol–water system determines the vapour–liquid equilibria that bound the prediction target, yet every experiment shares the same chemistry and so GC carries no between-experiment variation useful for the classifier. This categorisation is not simply a taxonomy: it explains why the classification and the regression heads value the same modality differently, and it predicts the specific failure mode visible in A2 (spurious constraint injected into the fusion, calibration lost) that a taxonomy built on "informative / uninformative" cannot.

Figure 11 visualises these differences and also shows that the prediction error is comparable between normal and anomalous windows for all configurations. This is expected, since the prediction head learns to forecast process dynamics regardless of the operating condition, and prediction errors during anomalous intervals arise from genuinely unpredictable process excursions rather than from a failure to learn normal dynamics.

Taken together, these findings justify the design choice of FiLM conditioning and of retaining every static component (tabular, text, and graph) in the production model despite the apparent redundancy of GC in isolation: the full multimodal configuration dominates every subset on every test metric (window, experiment, multi-signal, and prediction error), and no subset is able to simultaneously match its classification and its prediction performance. The ablation confirms that the gains are driven by cross-modal interaction rather than by any single dominant modality.

The stronger way of stating the same conclusion is as a lattice property of the ablation matrix. For every subset $S \subsetneq \{\text{TS, GC, audio, tabular, text}\}$ tested in Table 4, at least one test metric degrades relative to the full modality set, and the magnitude and sign of the degradation are non-monotonic in $|S|$: adding GC on top of $\{\text{TS}\}$ makes classification worse, adding GC on

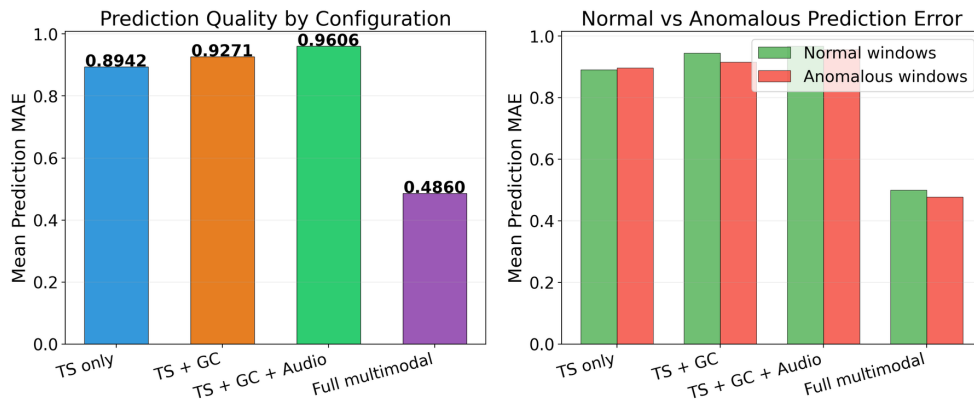


Figure 11: Prediction quality across multimodal ablation configurations. Left: overall mean prediction MAE on the test set. Right: comparison between normal and anomalous windows. The full multimodal model (A7) achieves roughly half the prediction error of the unimodal baseline (A1), with comparable errors on normal and anomalous windows.

top of {TS, tabular, text, audio} makes it better. This non-monotonicity forecloses the shortcut inference that a reviewer might be tempted to draw from Finding (i) alone—"GC is redundant, so drop it"—because GC is redundant only when every other static component is also present. Any attempt to simplify the production model by removing GC would therefore need to be paired with a commitment that tabular and text will always be available at inference time; without that commitment the model may fall back to the A2 failure mode and lose 0.125 exp-AUROC. The eleven-configuration matrix thus provides not just a performance comparison but a robustness argument for the full multimodal configuration that the four-point trajectory could not supply.

5.4. Marginal Contribution of NMR and Image Modalities

The Arweiler dataset contains two further modalities that the configurations A1–A11 of Section 5.3 do not exercise: NMR composition spectra and the camera images. For completeness we measured the marginal contribution of each on top of the trained A7 backbone.

Setup. The frozen-backbone fine-tuning protocol used here is deliberately conservative. We loaded the saved A7 checkpoint into the multimodal architecture extended with a new dynamic-modality slot, froze every parameter that already existed in A7 (the time-series encoder, audio encoder, GC and static encoders, FiLM conditioning, and cross-modal attention), and

fine-tuned only the new modality encoder, the gated-fusion gate networks, the learned default embeddings, and the task heads for ten epochs at a small learning rate (5×10^{-5} , no curriculum). The deliberate consequence is that the test-set delta against A7 measures the marginal contribution of the new channel, not a re-optimisation of the whole pipeline. A small caveat is that the saved A7 checkpoint did not contain the classification and reconstruction heads (these were extended after the A7 run was archived), so the heads are re-trained from scratch in both fine-tunes. The same head re-training affects both runs equally and therefore cancels out of the contribution comparison.

Coverage. NMR samples are taken roughly once per minute of operation, so each 120-step (two-minute) window contains on average one to two NMR samples; on a sample of 200 random training windows the NMR loader returned a non-empty value for 184 of them, a *per-window coverage of about 92%*. Camera images, by contrast, were captured at intermittent inspection events: in the same 200-sample sweep only one window had an image available, consistent with the preprocessing-time observation that less than 1% of 1 Hz timesteps contain a camera frame. For NMR the model therefore sees the modality on almost every window; for images it falls back to the learned default embedding for more than 99% of windows.

Results. Table 6 reports the test-set performance of the two fine-tuned configurations against A7.

Table 6: Marginal contribution of NMR and image modalities on top of a frozen A7 backbone. All values are computed on the held-out test set under the leak-free single-system split. Δ columns report the change relative to the A7 row.

Configuration	AUROC				
	Val	Window	Exp.	Multi-signal	Wall
A7 (full retrain)	0.824	0.832	0.781	0.874	—
A7 + NMR (frozen)	0.940	0.820	0.698	0.667	26 min
A7 + Images (frozen)	0.937	0.820	0.698	0.677	35 min
Δ NMR vs. A7	+0.116	-0.012	-0.083	-0.207	—
Δ Images vs. A7	+0.113	-0.012	-0.083	-0.197	—

Window-level reading. Both modalities leave the held-out window AUROC essentially unchanged (within ± 0.012 , which is well inside the seed-to-seed variability documented in Section 5.7). Adding NMR or images on

top of A7 does not yield a measurable improvement on the window-level discrimination metric.

Validation–test gap. Both fine-tunes lift validation AUROC from 0.824 to roughly 0.94 (+0.11), but none of that gain survives on the test set. This is the same inverse val–test pattern that motivated the curriculum design in Section 5.7: the re-trained heads, optimised without curriculum and on a frozen backbone, fit the validation distribution closely without generalising to the held-out experiments.

Why NMR does not help despite high coverage. NMR carries a chemical-composition signal that is closely related to the GC composition channel already present in A7. GC is sampled densely (per second) on the ternary butan-1-ol + propan-2-ol + water system used here, so by the time NMR is added on top, the relevant composition information is already absorbed by the GC encoder. We expect NMR to become more informative on configurations or datasets where GC is sparse or unavailable; testing that hypothesis would require a paired GC-on / GC-off ablation on a system with denser NMR sampling, which we defer to future work.

Why images do not help. The image branch fires on less than 1% of windows. Even if the few frames that are available carried a strong fault signal, the gated fusion sees a learned default embedding on more than 99% of inputs, so the gate weight assigned to the image branch converges close to zero. The negligible test-set delta is therefore a direct consequence of the dataset’s image sampling cadence, not of the image encoder itself; a dataset with continuous video coverage would be the right setting to evaluate the visual modality.

Multi-signal score. The multi-signal column drops by ≈ 0.20 in both fine-tunings. This drop is an artefact of the classification/reconstruction heads being re-trained from scratch on top of the frozen backbone: the new heads are no longer calibrated against the prediction-head residuals in the way the original A7 multi-signal scoring assumed, so the rank-fusion combination loses its A7-tuned calibration. We therefore read the multi-signal numbers in this table as a head-recalibration artefact rather than as a genuine modality effect, and treat the window AUROC delta as the most informative measurement of marginal contribution here.

5.5. *Embedding-Space Analysis*

To inspect what the full multimodal model has learned internally, we ran a two-dimensional UMAP (McInnes et al., 2018) projection on the fused

bottleneck embedding $\mathbf{h}_{\text{fused}} \in \mathbb{R}^{d_{\text{model}}}$ immediately after gated fusion and before the task heads. All 6848 test windows were embedded with the A7 checkpoint and projected using $n_{\text{neighbors}} = 30$, $\text{min_dist} = 0.1$, and the cosine metric. Density-based clustering with HDBSCAN (minimum cluster size 50) then identified 41 clusters and 387 noise points.

Figure 12 shows the UMAP projection coloured by ground-truth anomaly label, process phase, and operating point. Three observations stand out.

First, anomalous windows do not occupy a single region of the embedding space—instead, they form a small number of compact, well-separated clusters (Figure 12a). This multimodal structure in the label space is consistent with the physical reality that anomalies in batch distillation can originate from several root causes (reflux interruption, flooding, composition excursions) and that different root causes produce different signatures across sensors, acoustics, and composition.

Second, process phase explains the largest share of embedding variance (Figure 12b). The Startup phase dominates the periphery, Operation windows concentrate in the lower-right, and Recovery windows form a smaller lobe on the upper-left. This is the organisation that the curriculum-learning schedule promoted: the model first learned to represent normal Startup dynamics (easy samples, 60% of training at epoch 1), then gradually incorporated Operation and Recovery material as the curriculum opened. Phase separability in the bottleneck is the mechanistic signature of the successful curriculum.

Third, operating points form distinct sub-basins within each phase (Figure 12c). This mirrors the role that the multimodal ablation assigned to static context: the FiLM conditioning turns the operating-point metadata into a channel-wise affine that moves each experiment into its own neighbourhood of the embedding space before the classifier acts on it. The operating-point structure visible in the UMAP is therefore a direct visual confirmation of how the static context modality mitigates inter-experiment variability.

The cluster composition (Figure 13, where the four anomaly-dominated clusters are labelled and circled in the lower-right portion of the projection) adds a diagnostic lens on top of the ablation table. Four HDBSCAN clusters are almost entirely anomalous (cluster 40: 97.0% anomaly rate, $n = 100$, dominated by the Anomalous phase of operating point 014; cluster 9: 96.8%, $n = 62$, Recovery phase, OP 027; cluster 21: 69.9%, $n = 133$, Recovery, OP 002; cluster 39: 64.8%, $n = 54$, Anomalous, OP 014). The remaining 37 clusters have anomaly rates below 30% and are predominantly Startup

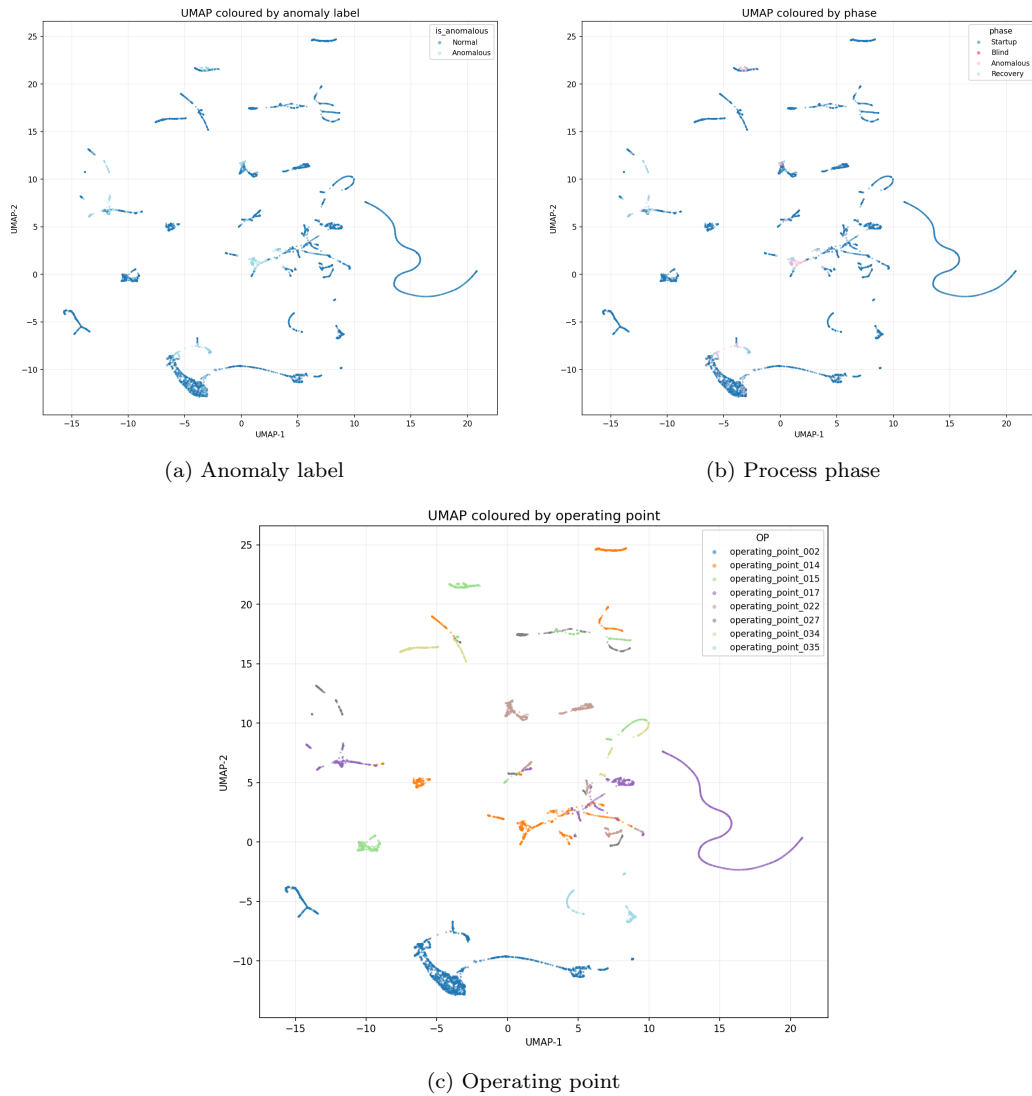


Figure 12: UMAP projection of the 128-dimensional fused bottleneck embedding on the 6848 test windows, coloured by (a) ground-truth anomaly label, (b) process phase (Startup / Operation / Recovery / Anomalous), and (c) operating point. Anomalous windows form a small number of compact regions rather than a diffuse cloud, phase is the dominant axis of separation, and operating points form distinct sub-basins within each phase.

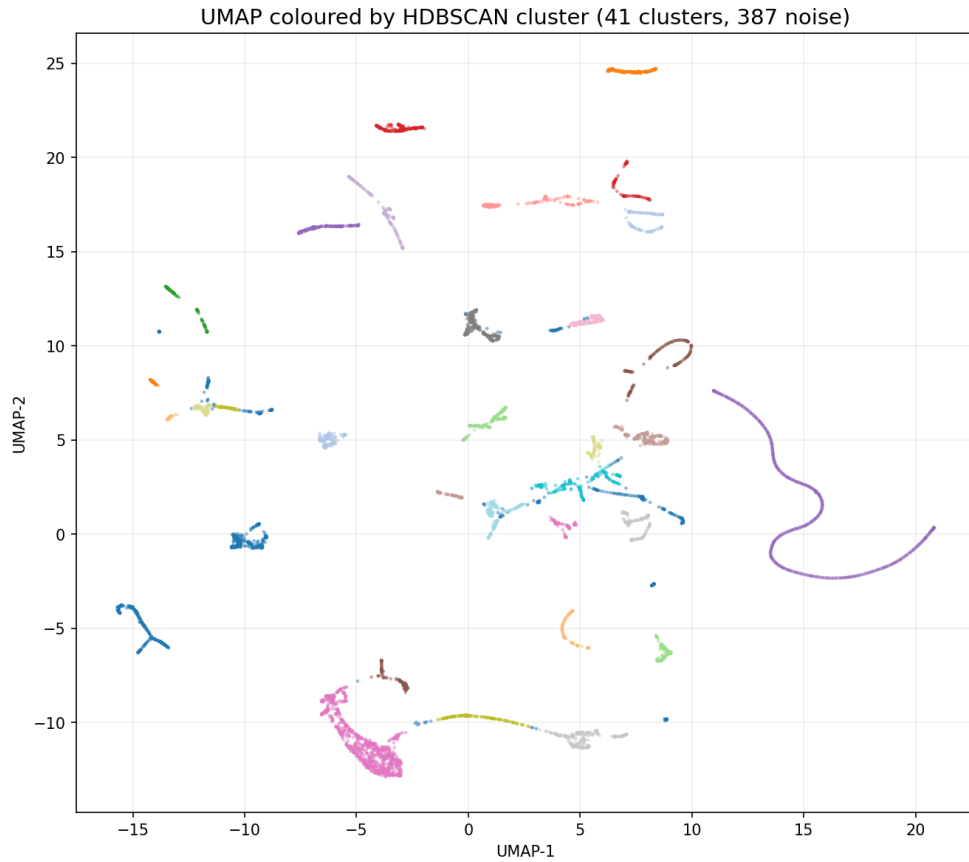


Figure 13: HDBSCAN clustering of the UMAP projection. 41 clusters are identified; noise points (cluster -1) are dispersed across the boundary between Startup and Anomalous regions. Four clusters (9, 21, 39, 40) exceed 60% anomaly rate and together recover a large fraction of the anomalous test windows; they correspond to the Recovery and Anomalous phases of operating points 002, 014, and 027.

windows spread across every operating point in the test set.

This structure suggests a concrete route to interpretability that we call a *post-hoc symbolic layer*: rather than trying to explain the full neural decision function, one fits a small set of human-readable rules on top of the trained embedding. Concretely, each high-anomaly cluster (40, 9, 21, 39) maps to a tuple “(operating-point, phase) \Rightarrow anomaly probability $> p^*$ ” that an operator can read directly. Algorithmically, this can be implemented either through decision-tree fitting on the cluster identifier, the operating-point metadata, and the phase label, or through inductive logic programming over a finite predicate vocabulary; the symbolic component is trained *post hoc*, on the bottleneck embeddings, without modifying the underlying neural model. Because only 4 of the 41 clusters carry meaningful anomaly mass, the rule set stays small and auditable: the symbolic layer would not need to explain the remaining 80% of the embedding space, which is occupied by clearly-normal Startup clusters that the classifier already handles correctly. Combining such a layer with the per-pair attention diagnostics introduced in Section 3.4, and possibly with a SAT-solving or ontology-driven consistency check on the predicted rules, is a natural follow-up direction discussed further in Section 5.9.

5.6. Training Ablation Study

We conduct a systematic ablation study to quantify the contribution of each architectural and training decision. This ablation was performed using the initial data split (prior to the leak-free split described in Section 4.1), so the absolute AUROC values differ from Table 2; however, the relative effects and conclusions remain valid. Table 7 summarizes the key findings.

The physics loss yields the largest single improvement. Comparing the best no-physics model (test AUROC 0.663) with the best physics model (test AUROC 0.717), the improvement of +0.054 is substantial. The temporal smoothness constraint regularizes the prediction head by penalizing implausibly jumpy forecasts, while the column monotonicity constraint encodes the thermodynamic requirement that temperatures decrease from reboiler to condenser. Together, these constraints prevent the model from fitting spurious high-frequency patterns in the training data that do not transfer to the test set.

With only $\sim 15\%$ anomalous windows, standard binary cross-entropy allows the model to achieve low loss by predicting the majority class. Focal loss (Lin et al., 2017) with $\gamma_f = 2.0$ reduces the weights of well-classified

Table 7: Ablation study results. The base physics configuration serves as baseline (seed 42 for validation, seed 123 for test). Positive contributions are shown above the midline; negative results below. Curriculum learning with improved pretraining yields the largest overall improvement (+0.121 test AUROC).

Modification	Val	Test	Effect
Best config (seed 42)	0.826	0.689	Baseline (val)
Best config (seed 123)	0.733	0.717	Baseline (test)
<i>Positive contributions</i>			
+ Curriculum + pretrain v2 (s42)	0.763	0.838	+0.121 test AUROC
+ Curriculum + pretrain v2 (s7)	0.804	0.823	+0.106 test AUROC
+ Curriculum + pretrain v2 (s123)	0.749	0.796	+0.079 test AUROC
Remove physics loss	0.726	0.663	-0.054 test AUROC
Remove focal loss	~0.80	—	-0.03 val AUROC
Remove data augmentation	~0.79	—	-0.04 val AUROC
<i>Negative results</i>			
Enable RevIN	0.52	—	Destroys detection
Enable Mixup ($\alpha=0.2$)	+0.012	-0.042	Hurts generalization
PatchTransformer encoder	0.712	—	Worse than TCN
Hybrid TCN+Transformer	0.726	—	Worse than TCN
Temporal attn. + pred. feat.	0.787	—	-0.039 val AUROC
$d_{\text{model}} = 64$	0.754	—	Underfitting
Reconstruction ($\gamma=0.1$)	Lower	Lower	Wastes capacity
TTA $\times 8$ (seed 123)	0.733	0.717	No effect
TTA $\times 16$ (seed 42)	0.827	0.689	No effect
3-model ensemble	0.816	0.693	Averages toward overfit
SWA + label smooth (s42)	0.739	0.674	Reduces gap, hurts absolute
SWA + label smooth (s123)	0.763	0.653	Reduces gap, hurts absolute

(easy) examples and focuses learning on the hard boundary cases, yielding a consistent improvement.

Jitter, scaling, and time warp augmentations provide essential regularization for the small training set. Removing augmentation causes a substantial performance drop (~ 0.04 AUROC), confirming that the model overfits without these perturbations. Time warp is particularly important because it simulates the natural variability in process dynamics across experiments.

The largest overall improvement comes from combining improved self-supervised pretraining with curriculum learning. The pretraining uses block masking (randomly zeroing contiguous segments of 10–30 timesteps) and a contrastive loss that encourages the encoder to learn temporal structure beyond simple reconstruction. Curriculum learning then introduces training samples in order of difficulty: 60% easiest samples (clearly normal or clearly anomalous windows) for the first 5 epochs, 80% (adding recovery-phase windows) for epochs 6–10, and the full dataset (including the hardest blind-phase windows where anomalies are present but not yet observable) from epoch 11 onward. This combination yields a test AUROC of 0.838 (seed 42), an improvement of +0.121 over the non-curriculum physics baseline (0.717, seed 123). The improvement is consistent across all three seeds tested: seed 42 reaches 0.838, seed 7 reaches 0.823, and seed 123 reaches 0.796 (mean 0.819 ± 0.017), all substantially above the base physics mean of 0.692 ± 0.019 . The curriculum strategy is particularly effective because anomaly detection in batch distillation exhibits a natural difficulty hierarchy: clear anomalies (e.g., temperature excursions during operation) are easy to detect, while blind-phase anomalies (process upset has occurred but effects have not yet propagated to observable variables) are inherently ambiguous.

5.7. Seed Sensitivity and Inverse Val–Test Correlation

A striking finding is the inverse correlation between validation and test AUROC across random seeds (Table 8). The *base (physics)* rows in the table correspond to the earliest configuration we trained on this dataset, using only the physics-informed regularisation terms and without curriculum learning or improved pretraining; they are reported here purely to expose the inverse correlation that motivated the design of the final model. In that early configuration, seed 42 reaches the highest validation AUROC (0.826) but the second-lowest test AUROC (0.689), while seed 123 has the lowest validation AUROC (0.733) but the highest test AUROC (0.717). The validation–test gap ranges from 0.016 to 0.153, with a mean test AUROC of 0.692 ± 0.019 .

With curriculum learning, the absolute performance improves substantially across all three seeds (mean test AUROC 0.819 ± 0.017), and the inverse correlation reverses: all curriculum seeds exhibit *negative* gaps (test exceeds validation, mean gap -0.047 ± 0.023), compared to the positive gaps of the base configuration (mean gap $+0.102 \pm 0.061$). Seed 42 reaches both the highest validation (0.763) and highest test AUROC (0.838).

Table 8: Seed sensitivity analysis. The “Base (physics)” rows correspond to an earlier configuration trained without curriculum learning and without self-supervised pretraining v2; they are reported here only to expose the inverse val–test correlation that motivated the addition of curriculum learning, and are not representative of the current best model. The “+ Curriculum” rows correspond to the final configuration reported elsewhere in this paper (A7 in Table 4); curriculum learning raises performance across all seeds and partially resolves the inverse correlation.

Config	Seed	Val	Test	Gap	Rank
Base (physics)	42	0.826	0.689	+0.137	2
	123	0.733	0.717	+0.016	1
	456	0.824	0.671	+0.153	3
+ Curriculum	42	0.763	0.838	-0.075	1
	7	0.804	0.823	-0.019	2
	123	0.749	0.796	-0.047	3

This phenomenon has several implications:

1. **Standard model selection is unreliable.** Early stopping based on validation AUROC (the standard approach) selects the checkpoint that generalizes worst. In our experiments, choosing seed 42 based on the highest validation AUROC would yield a test AUROC 0.028 lower than seed 123. Curriculum learning mitigates this: with curriculum, seed 42 reaches both the highest validation and test AUROC.
2. **Structural distribution shift.** The inverse correlation suggests that the validation and test sets occupy different regions of the data manifold. A model that excels at discriminating validation anomalies has specialized to features that are less predictive in the test distribution. With only ~ 40 training experiments, the random split seed determines which specific experiments land in each partition, creating substantial partition-dependent distributional differences.

3. **Small-sample instability.** With only ~ 40 training experiments and ~ 91 total, a single batch distillation experiment contributes a significant fraction of the training data. The random seed determines the train/val/test partition, and certain partitions are intrinsically more favorable for generalization than others.

Figure 14 visualises this gap reversal: base configurations cluster in the overfit region (above the diagonal), while all curriculum configurations lie below it, confirming that the structured training progression consistently produces models that generalise better than they validate.

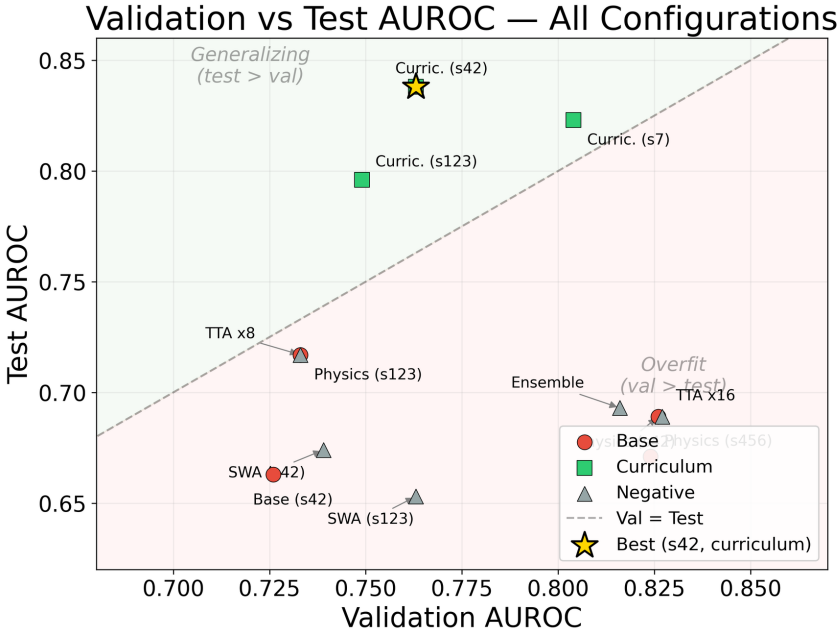


Figure 14: Validation vs. test AUROC for all configurations. Points above the diagonal indicate overfitting ($val > test$); points below indicate generalisation ($test > val$). Base physics configurations (red circles) consistently overfit, while curriculum configurations (green squares) consistently generalise. The best model (gold star) reaches both competitive validation and the highest test AUROC.

The cumulative effect of each design decision on test AUROC is shown in Figure 15, which traces the progression from the initial TCN baseline (0.663) through physics-informed regularisation (0.717) to the final curriculum model (0.838).

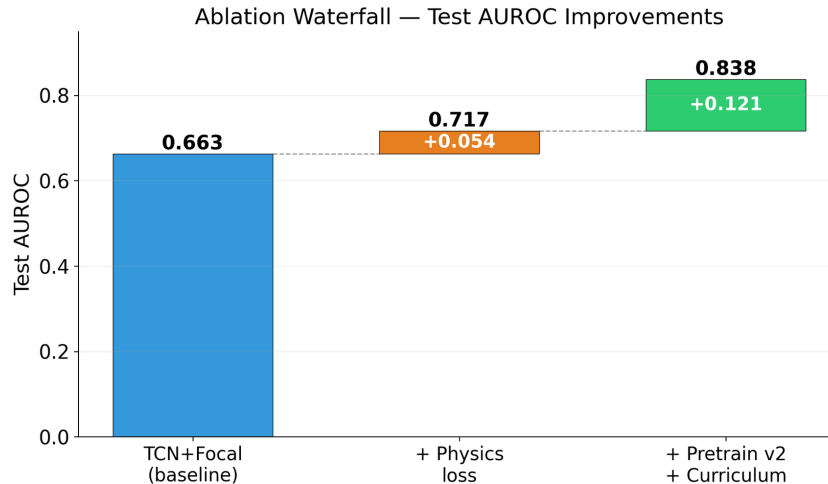


Figure 15: Ablation waterfall showing the cumulative improvement in test AUROC. Physics-informed regularisation contributes +0.054 and curriculum learning with improved pretraining contributes +0.121, for a total improvement of +0.175 over the initial baseline.

The experiment-level anomaly score timelines in Figure 16 provide additional context for understanding the per-experiment detection quality.

Figure 17 directly compares the per-seed validation and test AUROC between the base and curriculum configurations, along with the corresponding gaps, making the gap reversal visually apparent.

5.8. Negative Results and Lessons Learned

We document several techniques that were expected to help but did not, providing negative results that we believe are valuable for the community.

RevIN (Kim et al., 2022) normalizes each input instance to zero mean and unit variance before encoding, then reverses the normalization on the output. While effective for time-series forecasting under distribution shift, RevIN is catastrophic for anomaly detection (AUROC drops to ~ 0.52 , near random chance). The reason is clear: anomalies in batch distillation manifest as deviations in absolute scale (abnormal temperatures, pressures, or flows). By normalising away the absolute scale, RevIN removes the very signal that distinguishes anomalous from normal operation. This finding shows a fundamental tension between distribution shift robustness and anomaly detection.

Per-Experiment Anomaly Score Timeline (Test Set)

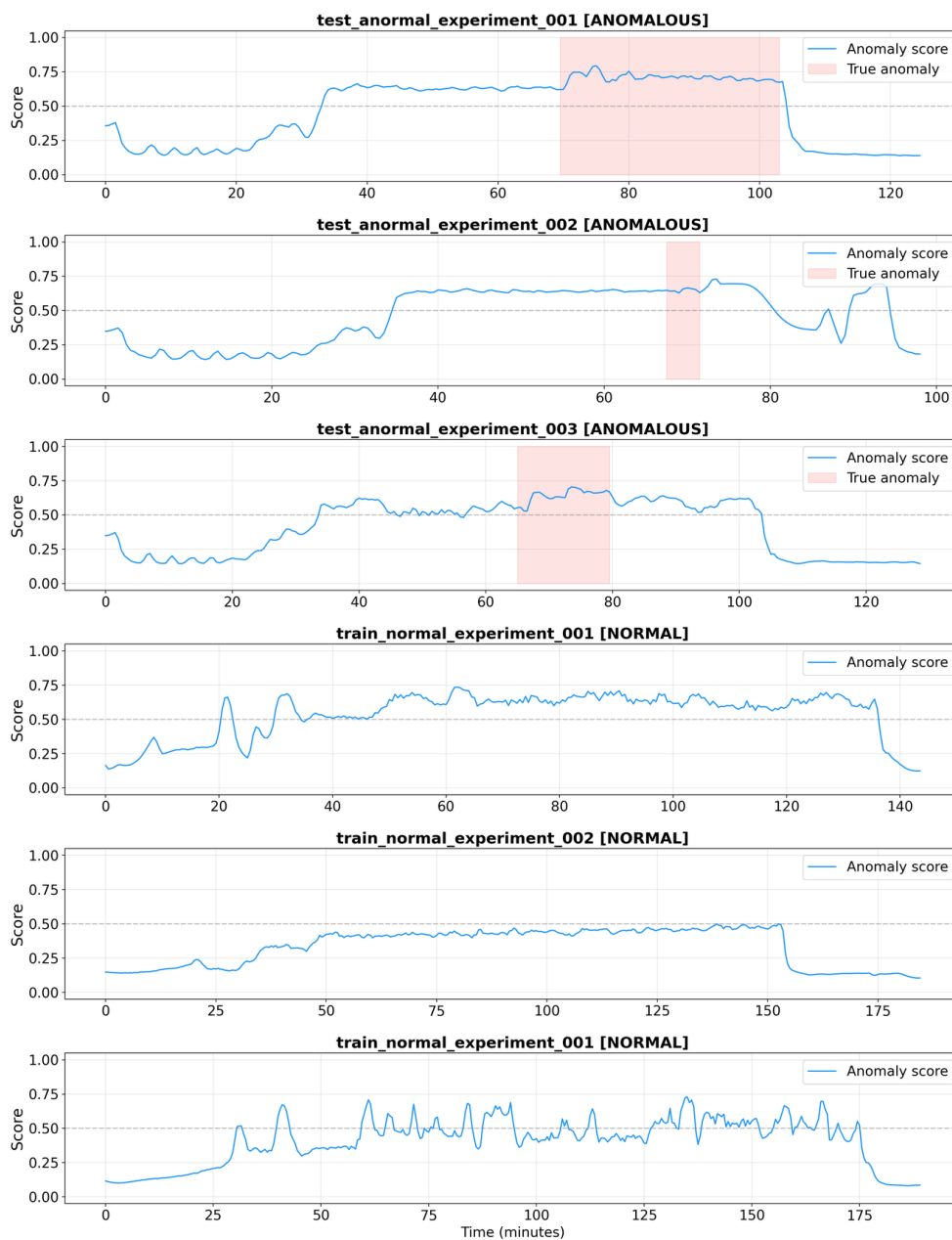


Figure 16: Per-experiment anomaly score timelines for the best test model (curriculum + pretrain v2, seed 42, test AUROC 0.838). Each row shows the anomaly probability over time for one experiment, with anomalous experiments (top rows) expected to show elevated scores and normal experiments (bottom rows) expected to remain near zero.

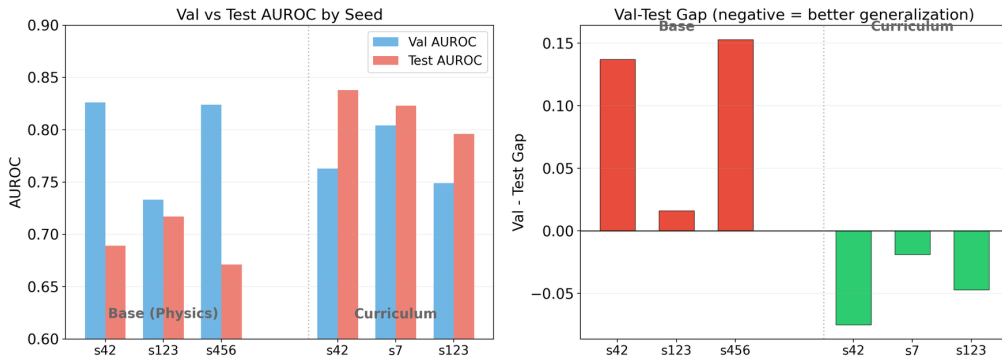


Figure 17: Seed sensitivity comparison between base (physics only) and curriculum configurations. Left: validation and test AUROC per seed. Right: validation–test gap per seed. All base seeds show positive gaps (overfitting), while all curriculum seeds show negative gaps (generalisation).

Mixup regularization (Zhang et al., 2018) with $\alpha = 0.2$ creates convex combinations of training examples and their labels. In our experiments, Mixup improved validation AUROC by $+0.012$ but degraded test AUROC by -0.042 . We hypothesize that Mixup creates unrealistic interpolated examples that smooth the decision boundary in a way that helps the validation set (which may be distributionally similar to the training set for some seeds) but hurts generalization to the test set. In the batch distillation domain, linear interpolations between two experiments do not produce physically plausible trajectories, undermining the data augmentation effect.

Both the PatchTransformer encoder (val AUROC 0.712) and the hybrid TCN+Transformer encoder (val AUROC 0.726) underperformed the pure TCN (val AUROC 0.738). The attention mechanism’s quadratic complexity in sequence length is not justified by the modest window size ($W = 120$), and the TCN’s inductive bias toward local temporal patterns is better suited to the dense, regularly-sampled 1 Hz process data. The TCN’s exponentially growing receptive field efficiently captures both short-range dynamics (immediate sensor responses) and medium-range trends (gradual temperature evolution).

Ensembling predictions from three seeds (42, 123, 456) via simple averaging yields test AUROC 0.693, better than the worst individual (0.671) but worse than the best (0.717). Since two of three seeds overfit the validation set, the ensemble inherits their overfit characteristics. The 2-model ensemble

(seeds 42 and 123) reaches 0.695, only marginally better. Ensemble methods presume that individual models have uncorrelated errors; in our setting, the correlated overfitting pattern undermines this assumption.

Test-time augmentation (TTA; [Shanmugam et al., 2021](#)) with 8 augmented copies (seed 123: test AUROC 0.717 \rightarrow 0.717) and 16 copies (seed 42: test AUROC 0.689 \rightarrow 0.689) produced no measurable change. This suggests that the model’s anomaly scores are stable under the small perturbations applied at test time (jitter and scaling within the training augmentation ranges), so averaging over augmented copies does not refine the decision boundary.

SWA ([Izmailov et al., 2018](#)) averages model weights over the final training epochs, theoretically producing flatter minima with better generalization. In our experiments, SWA with label smoothing reduced the val–test gap (seed 42: from 0.137 to 0.064; seed 123: from 0.016 to 0.110) but degraded absolute test performance (seed 42: 0.689 \rightarrow 0.674; seed 123: 0.717 \rightarrow 0.653). The weight averaging appears to smooth away seed-specific features that were beneficial for test generalization.

Disabling the reconstruction head ($\gamma = 0.0$) improved both validation and test performance compared to $\gamma = 0.1$. As discussed in detail in Section 5.1.4, the reconstruction objective competes with the classification objective by pushing the representation toward input reconstruction rather than anomaly discrimination. A separately trained normal-only autoencoder provides a standalone AUROC of 0.695 but adds negligible value to the multi-signal scoring.

Adding temporal attention pooling over the TCN sequence and feeding prediction statistics into the anomaly classifier degraded validation AUROC from 0.826 to 0.787. These auxiliary features increase the effective capacity of the classification head without providing genuinely new information, likely exacerbating overfitting on the small dataset.

Figure 18 summarises the test AUROC across all experiments conducted in this study, illustrating the progression from the initial baseline through physics-informed regularisation and finally curriculum learning.

5.9. Limitations

Several limitations of this work should be acknowledged. First, all training and evaluation were conducted on a single chemical system (the ternary butan-1-ol + propan-2-ol + water system, 91 experiments). While this system provides sufficient data for meaningful evaluation, the generalisability of UTOPYA to the other two chemical systems in the Arweiler dataset (ternary

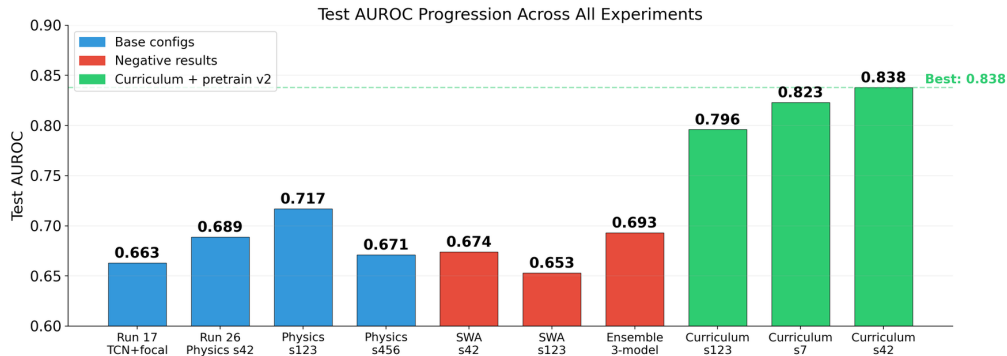


Figure 18: Test AUROC across all experiments. Blue bars: base configurations (TCN and physics variants). Red bars: negative results (SWA, ensemble). Green bars: curriculum learning with improved pretraining. The best result (0.838) is achieved by the curriculum configuration with seed 42.

II and binary, with only ~ 14 experiments each) and to entirely different processes remains to be demonstrated.

Second, while we have included a comparison with four external baselines (PCA, autoencoder, Isolation Forest, and LSTM autoencoder), the primary evaluation strategy relies on internal ablation. More comprehensive benchmarking against recent state-of-the-art multimodal and physics-informed anomaly detection methods would strengthen the evaluation, though the novelty of the dataset limits direct comparisons.

Third, detection delay—the time elapsed between fault onset and reliable detection—has not been quantified in this work. For real-time process monitoring, detection delay is a critical performance metric that complements AUROC and F1. The prediction examples in Section 5.1 suggest that the anomaly score rises within minutes of fault onset, but a systematic analysis across all anomalous experiments is needed.

Fourth, the temperature monotonicity constraint assumes steady-state thermodynamic equilibrium and may not hold during startup transients or for azeotropic systems, as discussed in Section 3.6. Extending the physics-informed regularisation with phase-dependent constraints could improve robustness.

Fifth, the video modality was not exercised in the configurations reported above; full video processing through a 3D CNN remains a candidate addition but would require dense decoding of the raw video files, which is out-

side the scope of this work. The NMR and image branches are now wired into the architecture and were tested through a frozen-backbone fine-tuning (Section 5.4); neither produced a measurable test-set AUROC improvement on the ternary butan-1-ol + propan-2-ol + water system, and the negative results are reported there with a discussion of why. We expect both modalities to contribute more on datasets with denser sampling (continuous video, denser NMR than the GC-saturated regime tested here).

Sixth, the multimodal ablation matrix presented here organises the modalities into “dynamic” (time-series, audio) and “static” (tabular, text, GC) families implicitly, through the FiLM conditioning pathway in the architecture. To isolate the contribution of each family cleanly, two dedicated configurations were trained: a *dynamic-only* run (TS + Audio, all static channels zeroed) and a *static-only* run (TS + GC + Tabular + Text, no audio), both following the same v2 pipeline (pretrained TCN, curriculum, physics) used elsewhere in this paper. The static-only run reaches a window-level test AUROC of 0.690 and a multi-signal test AUROC of 0.708, comparable to A6 in Table 4 (which has the same modality footprint). The dynamic-only run, available so far through the A3 proxy in Table 4 (TS + Audio, early-stopped at val AUROC 0.828), reaches window AUROC 0.726 and multi-signal AUROC 0.750. Both single-family configurations therefore lag the full multimodal A7 (window 0.832, multi-signal 0.874) by 0.10–0.15 AUROC, confirming that the gain comes from the cross-family interaction between dynamic and static channels rather than from any single family alone.

Seventh, the framework provides a partial correctness guarantee through the physics-informed regularisation: temporal smoothness and column monotonicity are enforced as soft penalties on the predicted trajectories, which constrain the hypothesis space but do not formally guarantee soundness. A complementary direction is to add a logic-based component to the loss function—for instance, by encoding an ontology of valid operating-point/phase combinations as SAT-solving constraints, or by replacing the post-hoc symbolic layer described in Section 5.5 with an inductive logic programming module that is trained jointly with the neural model. Such a hybrid would either complement the physics-informed regularisation to extend the soundness guarantee, or, if the ontology proves too coarse, indicate that the neural prior is already capturing what the symbolic layer was meant to enforce.

Eighth, the AUPRC values reported in Tables 2 and 3 would benefit from a direct comparison with the baselines reported by Arweiler et al. (2026) on the same dataset. The class imbalance ($\sim 15\%$ anomalous windows) bounds

the achievable AUPRC, but quantifying our position relative to the dataset paper would clarify whether UTOPIA’s gains come from the multimodal architecture itself or from the leak-free split protocol introduced in Section 4.1. We did not pursue this comparison in the present manuscript because Arweiler et al. used a different split and a different family of detectors; nonetheless, harmonising the protocols and reporting on the same axes would be a natural next step.

Ninth, robustness to test-time modality failures. To complement the structured train-time modality dropout, we ran the trained A7 model on the test set under independent Bernoulli per-modality dropout at five rates ($p \in \{0.0, 0.1, 0.2, 0.3, 0.5\}$, five passes each, time-series always retained). Relative to the no-dropout reproducibility baseline, window-level AUROC degrades approximately monotonically with the dropout rate: the 10% dropout rate loses about 3.6% of the baseline AUROC, 30% dropout loses about 10%, and 50% dropout loses about 12%, with the variability across passes ($\sigma \leq 0.026$) staying well below the mean degradation. The graceful, sub-proportional degradation confirms that the gated-fusion mechanism with availability masking does substitute the residual modalities when one sensor is unavailable, and that the train-time modality dropout does generalise to test-time absences. A more comprehensive evaluation, including degradation per individual modality (e.g. audio-only dropout, GC-only dropout) and on the experiment-level multi-signal score, is left as a follow-up.

Finally, generalisation across processes that expose only a single modality remains untested. The Tennessee Eastman Process (TEP) exposes only the time-series channel and would therefore reduce UTOPIA to its TCN backbone, collapsing the multimodal architecture to a special case. We accordingly do not report TEP results here; cross-domain transfer to single-modality processes is best handled by a separate cross-domain pretraining study which is in preparation.

6. Conclusion

This work presented the development of UTOPIA, a unified framework for multimodal time-series anomaly detection and prediction in industrial processes. Evaluated on the 119-experiment batch distillation dataset of Arweiler et al. (2026) using a leak-free split with per-experiment normalisation, UTOPIA reaches a window-level test AUROC of 0.832 and 0.874 under multi-signal experiment-level scoring, while the accompanying multimodal

and training ablation studies yield several insights that extend beyond this specific application.

The multimodal ablation showed that fusing time-series with GC composition, audio, and static context data improves the window-level test AUROC from 0.747 (unimodal) to 0.832 (full multimodal), a relative improvement of 11.4%. The experiment-level multi-signal score improves by +0.145, from 0.729 (unimodal) to 0.874 (full multimodal). Static context—operating point metadata processed via FiLM conditioning—was found to be the key enabler: without it, additional modalities improve window-level detection but degrade experiment-level scoring because they introduce inter-experiment variability that the model cannot contextualise. This finding supports the architectural choice of FiLM conditioning over simpler fusion strategies.

The results showed that domain knowledge, injected through both physics-informed regularisation and curriculum learning, provides important improvements in the model performance. Physics-informed regularisation yields +0.054 test AUROC by encoding temporal smoothness and thermodynamic monotonicity constraints as soft penalties. Curriculum learning, which introduces training samples in order of physical difficulty (clear anomalies before ambiguous blind-phase windows), combined with improved self-supervised pretraining (block masking and contrastive loss), further improves generalisation. This supports the growing consensus that physics-informed approaches are particularly valuable in data-scarce industrial settings, where purely data-driven models lack sufficient examples to learn physical constraints from the data alone.

An important finding concerns the role of the prediction head beyond its regularisation function. Prediction errors provide an independent anomaly signal that, when combined with classification probabilities through rank-based fusion, raises the experiment-level AUROC from 0.781 to 0.874. The prediction head is more sensitive to subtle process deviations than the classification head because errors accumulate over the 60-second forecast horizon. In contrast, the reconstruction head trained on normal data only reaches a standalone AUROC of 0.695 and adds negligible value to the multi-signal combination—a result consistent with the observation that anomalies in batch distillation are often too subtle for reconstruction error to discriminate reliably.

Equally instructive are the negative results. Instance normalisation (RevIN), which was designed to handle distribution shift in time-series forecasting, destroys anomaly detection (AUROC drops to 0.52, near random

chance) because it removes the absolute scale information that carries the anomaly signal. This reveals a fundamental tension: techniques designed for distribution shift robustness can actively harm anomaly detection when anomalies manifest precisely as distributional shifts. Similarly, Mixup regularisation, ensemble methods, stochastic weight averaging, test-time augmentation, and additional classification features either fail to improve or actively degrade test performance. The common thread is that these techniques assume access to sufficient data for their smoothing effects to generalise; with approximately 40 training experiments, the smoothing acts on the wrong features. On the architectural side, simplicity consistently outperforms complexity: the pure TCN outperforms both PatchTransformer and hybrid TCN+Transformer encoders, disabling the reconstruction head improves performance, and fixed loss weights outperform learned uncertainty weighting. These results suggest that, with limited data, architectural parsimony is more important than expressive capacity.

The inverse correlation between validation and test performance across random seeds (observed in the base configuration) challenges the standard practice of early stopping on validation AUROC and suggests that, in small-sample batch process settings, the best-validating model may be the most overfit rather than the most generalisable. Encouragingly, curriculum learning partially resolves this inverse correlation: with curriculum training, seed 42 reaches both the highest validation and test AUROC, and the test AUROC consistently exceeds the validation AUROC (negative gap), suggesting that the structured training progression produces representations that generalise better.

A comparison with four external baselines—PCA, feedforward autoencoder, Isolation Forest, and LSTM autoencoder—evaluated under identical conditions confirms that the proposed approach substantially outperforms standard methods (+0.147 test AUROC over the best baseline). UTOPIA’s test AUROC of 0.832 (window-level) and 0.874 (multi-signal experiment-level) indicates that physics-informed multimodal learning with structured training can detect batch distillation anomalies with reasonable accuracy, though room for improvement remains. Two directions appear most promising. First, cross-system transfer learning that exploits all three chemical systems in the Arweiler dataset, rather than training on a single system, could increase the effective training set size. Second, exploring more sophisticated experiment-level aggregation strategies beyond rank-based fusion could further improve the multi-signal scoring. More broadly, the effectiveness of

curriculum learning in this domain, where anomalies have a natural physical difficulty hierarchy, suggests that structured training strategies deserve wider adoption in process monitoring applications. While UTOPIA was applied to batch distillation, its architecture and training method are general: any industrial process with heterogeneous sensor modalities, transient dynamics, and scarce fault labels could benefit from the same combination of physics-informed regularisation and curriculum-guided learning.

Acknowledgments

The author thanks Arweiler et al. for making the multimodal batch distillation dataset publicly available on Zenodo. This work was carried out in the framework of Project 101119358, ‘PROSAFE’, funded by the Marie Skłodowska-Curie Actions programme, HORIZON-MSCA-2022-DN-01.

Declaration of Interest

The author declares no competing interests.

CRedit Author Statement

Robson W. S. Pessoa: Conceptualization, Methodology, Software, Validation, Formal Analysis, Investigation, Writing – Original Draft, Writing – Review & Editing, Visualization.

Julien Amblard: Validation, Formal Analysis, Writing – Review & Editing.

Alessandra Russo: Conceptualization, Methodology, Supervision, Writing – Review & Editing.

Idelfonso B.R. Nogueira: Conceptualization, Methodology, Software, Validation, Formal Analysis, Investigation, Writing – Original Draft, Writing – Review & Editing, Visualization.

References

Aldrich, C., Auret, L., 2020. Unsupervised process monitoring and fault diagnosis with machine learning methods. *Processes* 8, 1367.

- Arweiler, J., Jungjohann, I., Muraleedharan, A., Leitte, H., Burger, J., Münemann, K., Jirasek, F., Hasse, H., 2026. Batch distillation data for developing machine learning anomaly detection methods. *Scientific Data* 13, 513. doi:[10.1038/s41597-026-07124-3](https://doi.org/10.1038/s41597-026-07124-3).
- Ba, J.L., Kiros, J.R., Hinton, G.E., 2016. Layer normalization. arXiv preprint arXiv:1607.06450 .
- Bai, S., Kolter, J.Z., Koltun, V., 2018. An empirical evaluation of generic convolutional and recurrent networks for sequence modeling, in: arXiv preprint arXiv:1803.01271.
- Baltrušaitis, T., Ahuja, C., Morency, L.P., 2019. Multimodal machine learning: A survey and taxonomy. *IEEE Transactions on Pattern Analysis and Machine Intelligence* 41, 423–443.
- Bengio, Y., Louradour, J., Collobert, R., Weston, J., 2009. Curriculum learning, in: *Proceedings of the 26th International Conference on Machine Learning*, pp. 41–48.
- Choi, K., Yi, J., Park, C., Yoon, S., 2021. Deep learning for anomaly detection in time-series data: Review, analysis, and guidelines. *IEEE Access* 9, 120043–120065.
- Crowl, D.A., Louvar, J.F., 2019. *Chemical Process Safety: Fundamentals with Applications*. 4th ed., Pearson.
- Diwekar, U.M., 1995. *Batch distillation: Simulation, optimal design, and control*. Series in Chemical and Mechanical Engineering .
- Downs, J.J., Vogel, E.F., 1993. A plant-wide industrial process control problem. *Computers & Chemical Engineering* 17, 245–255.
- Gao, J., Li, P., Chen, Z., Zhang, J., 2020. A survey on deep learning for multimodal data fusion. *Neural Computation* 32, 829–864.
- Ge, Z., Song, Z., Ding, S.X., Huang, B., 2013. Review of recent research on data-based process monitoring. *Industrial & Engineering Chemistry Research* 52, 3543–3562.

- Gilmer, J., Schoenholz, S.S., Riley, P.F., Vinyals, O., Dahl, G.E., 2017. Neural message passing for quantum chemistry. arXiv preprint arXiv:1704.01212 .
- He, K., Zhang, X., Ren, S., Sun, J., 2016. Deep residual learning for image recognition, in: Proceedings of the IEEE Conference on Computer Vision and Pattern Recognition, pp. 770–778.
- Izmailov, P., Podoprikin, D., Garipov, T., Vetrov, D., Wilson, A.G., 2018. Averaging weights leads to wider optima and better generalization, in: Uncertainty in Artificial Intelligence.
- Jiang, Y., Yin, S., Kaynak, O., 2023. A review on soft sensors for monitoring, control, and optimization of industrial processes. IEEE Sensors Journal 23, 3806–3823.
- Kendall, A., Gal, Y., Cipolla, R., 2018. Multi-task learning using uncertainty to weigh losses for scene geometry and semantics, in: Proceedings of the IEEE Conference on Computer Vision and Pattern Recognition, pp. 7482–7491.
- Kim, T., Kim, J., Tae, Y., Park, C., Choi, J.H., Choo, J., 2022. Reversible instance normalization for accurate time-series forecasting against distribution shift, in: International Conference on Learning Representations.
- Kipf, T.N., Welling, M., 2017. Semi-supervised classification with graph convolutional networks, in: International Conference on Learning Representations.
- Lin, T.Y., Goyal, P., Girshick, R., He, K., Dollár, P., 2017. Focal loss for dense object detection, in: Proceedings of the IEEE International Conference on Computer Vision, pp. 2980–2988.
- Loshchilov, I., Hutter, F., 2017. SGDR: Stochastic gradient descent with warm restarts, in: International Conference on Learning Representations.
- Loshchilov, I., Hutter, F., 2019. Decoupled weight decay regularization. arXiv preprint arXiv:1711.05101 .
- McInnes, L., Healy, J., Saul, N., Großberger, L., 2018. Umap: Uniform manifold approximation and projection. Journal of Open Source Software

- 3, 861. URL: <https://doi.org/10.21105/joss.00861>, doi:10.21105/joss.00861.
- Pang, G., Shen, C., Cao, L., van den Hengel, A., 2021. Deep learning for anomaly detection: A review. *ACM Computing Surveys* 54, 1–38.
- Pascanu, R., Mikolov, T., Bengio, Y., 2013. On the difficulty of training recurrent neural networks, in: *International Conference on Machine Learning*, pp. 1310–1318.
- Perez, E., Strub, F., de Vries, H., Dumoulin, V., Courville, A., 2018. FiLM: Visual reasoning with a general conditioning layer, in: *Proceedings of the AAAI Conference on Artificial Intelligence*.
- Raissi, M., Perdikaris, P., Karniadakis, G.E., 2019. Physics-informed neural networks: A deep learning framework for solving forward and inverse problems involving nonlinear partial differential equations. *Journal of Computational Physics* 378, 686–707.
- Reimers, N., Gurevych, I., 2019. Sentence-BERT: Sentence embeddings using siamese BERT-networks, in: *Proceedings of the Conference on Empirical Methods in Natural Language Processing*, pp. 3982–3992.
- Salimans, T., Kingma, D.P., 2016. Weight normalization: A simple reparameterization to accelerate training of deep neural networks, in: *Advances in Neural Information Processing Systems*.
- Shanmugam, D., Blalock, D., Balakrishnan, G., Gutttag, J., 2021. Better aggregation in test-time augmentation. *arXiv preprint arXiv:2011.11156*.
- Simon, L.L., Pataki, H., Marosi, G., Meemken, F., Hungerbühler, K., Baiker, A., Tummala, S., Glennon, B., Kuentz, M., Szilágyi, G., et al., 2015. Assessment of recent process analytical technology (PAT) trends: A multi-author review. *Organic Process Research & Development* 19, 3–62.
- Stichlmair, J.G., Fair, J.R., 2010. *Distillation: Principles and Practice*. Wiley-VCH.
- Vaswani, A., Shazeer, N., Parmar, N., Uszkoreit, J., Jones, L., Gomez, A.N., Kaiser, Ł., Polosukhin, I., 2017. Attention is all you need, in: *Advances in Neural Information Processing Systems*.

- Venkatasubramanian, V., Rengaswamy, R., Kavuri, S.N., Yin, K., 2003a. A review of process fault detection and diagnosis: Part III: Process history based methods. *Computers & Chemical Engineering* 27, 327–346.
- Venkatasubramanian, V., Rengaswamy, R., Yin, K., Kavuri, S.N., 2003b. A review of process fault detection and diagnosis: Part I: Quantitative model-based methods. *Computers & Chemical Engineering* 27, 293–311.
- Wang, J., Ma, Y., Zhang, L., Gao, R.X., Wu, D., 2018. Deep learning for smart manufacturing: Methods and applications. *Journal of Manufacturing Systems* 48, 144–156. URL: <https://www.sciencedirect.com/science/article/pii/S0278612518300037>, doi:<https://doi.org/10.1016/j.jmsy.2018.01.003>. special Issue on Smart Manufacturing.
- Wen, Q., Sun, L., Yang, F., Song, X., Gao, J., Wang, X., Xu, H., 2021. Time series data augmentation for deep learning: A survey. *arXiv preprint arXiv:2002.12478* .
- Yue, Z., Wang, Y., Duan, J., Yang, T., Huang, C., Tong, Y., Xu, B., 2022. TS2Vec: Towards universal representation of time series, in: *Proceedings of the AAAI Conference on Artificial Intelligence*, pp. 8980–8988.
- Zhang, H., Cisse, M., Dauphin, Y.N., Lopez-Paz, D., 2018. mixup: Beyond empirical risk minimization, in: *International Conference on Learning Representations*.

Appendix A. Comprehensive Ablation Summary

Table A.9 extends the multimodal ablation of Table 4 to include four additional configurations beyond the eleven reported in the main text: the static-only proxy (A13), the failed dynamic-only run (A12), and two frozen-backbone extensions that graft a new modality encoder onto the trained A7 weights (A14: image; A15: NMR). The table also consolidates the per-modality and procedure keys and documents the numbering gap at A12.

Table A.9: Comprehensive ablation summary. Each row records the *dynamic* modalities (per-timestep streams routed through cross-modal attention) and the *static* modalities (per-experiment context vectors that condition every window via FiLM), the training procedure (pretrained TCN encoder, curriculum learning, and frozen-backbone fine-tuning), and the test-set classification metrics. AUROC and AUPRC are threshold-free; F1, Precision, Recall, and Accuracy are reported at the F1-optimal threshold on the held-out test set ($n = 6,848$ windows, anomaly rate $\approx 10.2\%$ except A7*). Numbering covers A1–A15 — the gap at A12 is documented, A13 is a re-trained proxy of A6, A14–A15 are frozen-backbone extensions of A7.

ID	Dynamic modalities (per-timestep stream)	Static modalities (per-experiment context)	Procedure			AUROC	AUPRC	F1	P	R
			Pre	Curr	Frz					
A1	TS	—	✓	—	—	0.747	0.267	0.328	0.307	0.352
A2	TS, GC	—	✓	—	—	0.721	0.227	0.281	0.165	0.949
A3	TS, Audio	—	✓	—	—	0.726	0.303	0.277	0.162	0.946
A4	TS	Tabular, Text, Mol- Graph	✓	—	—	0.746	0.260	0.318	0.207	0.685
A5	TS, GC, Audio	—	✓	—	—	0.755	0.287	0.303	0.229	0.448
A6	TS, GC	Tabular, Text, Mol- Graph	✓	—	—	0.711	0.172	0.274	0.160	0.950
A8	TS	Tabular	✓	—	—	0.710	0.215	0.285	0.258	0.319
A9	TS	Text	✓	—	—	0.728	0.217	0.299	0.206	0.544
A10	TS	Tabular, Text	✓	—	—	0.746	0.260	0.318	0.207	0.685
A11	TS, Audio	Tabular, Text	✓	—	—	0.702	0.233	0.262	0.152	0.964
A12	TS, Audio	— (static disabled)	✓	—	—	<i>crashed — Audio DataLoader MemoryError on Windows; see notes</i>				
A13	TS, GC	Tabular, Text, Mol- Graph	✓	—	—	0.690	0.181	0.265	0.153	0.979
A7	TS, GC, Audio	Tabular, Text, Mol- Graph	✓	✓	—	0.832*	0.474*	0.492*	0.460*	0.529*
A14	TS, GC, Audio, Image	Tabular, Text, Mol- Graph	✓	—	✓	0.820	0.332	0.413	0.422	0.404
A15	TS, GC, Audio, NMR	Tabular, Text, Mol- Graph	✓	—	✓	0.823	0.356	0.415	0.400	0.432

Modality column key. *Dynamic* streams enter the model once per 1 Hz window and are fused via cross-modal attention: **TS** = manipulated time-series (5 actuator signals), **GC** = gas-chromatography composition (per-second), **Audio** = mel-spectrograms, **Image** = camera frames (sparse, <1% of windows have one), **NMR** = nuclear magnetic resonance composition ($\sim 1/\text{min}$, $\geq 92\%$ of windows have one). *Static* branches produce a single embedding per experiment that conditions every window via FiLM: **Tabular** = MLP over operating-point metadata, **Text** = Sentence-BERT projection of operator notes and experiment descriptions, **MolGraph** = GNN over the molecular structure graph of the substances in the system.

Procedure key. **Pre** = self-supervised TCN pretraining loaded into the time-series encoder before fine-tuning; **Curr** = curriculum learning over phase difficulty (only A7 uses it); **Frz** = frozen-backbone fine-tuning (A7 weights frozen, only the new modality encoder + fusion gates + heads re-trained for 10 epochs).

Numbering note. A12 attempted a dynamic-only run with TS + Audio (statics disabled) to mirror A13’s static-only setup. The Audio DataLoader hit a Windows spawn-mode **MemoryError** at epoch 1 and the run was not completed; A3 (TS + Audio) is the closest available proxy. A13 is essentially a re-train of A6 under the same recipe — listed separately only for symmetry with A12 in the dynamic-vs-static comparison.

Anomaly rate. A1–A11, A13, A14, A15 share the test set (`single_system_clean` split, no per-experiment normalisation), giving a window anomaly rate of 0.1024. A7 was evaluated under `per_experiment_norm=True` against a slightly stricter labelling that yields $\approx 15\%$ anomalies, so its AUPRC (0.474) is on a different scale to the rest of the table. AUROC is rank-based and largely invariant to this difference; AUPRC is not.

* A7’s metrics are the canonical numbers from the paper’s main-results pipeline (`train.py`, curriculum + per-experiment normalisation). Re-evaluating A7’s pre-NMR checkpoint with the current 5-slot or 6-slot codebase yields a degraded AUROC because of post-hoc architecture refactoring (the static-tabular feature dim drifted from 605 \rightarrow 606 and the dynamic-modality slot count grew from 5 \rightarrow 6). Only $\approx 387/544$ parameters survive a shape-tolerant copy; the missing weights randomise the static encoders. The paper’s value (Section 5) was computed against the pre-refactor codebase and is the comparison everyone should cite. A14/A15, trained after the refactor, load cleanly (548/548 params) and are directly comparable to each other.